Reduction of aerodynamic noise from square bars by introducing spanwise waviness

X. W. Liu[a,b,*], Z. W. Hu[b], D. J. Thompson[a], V. Jurdic[c]

[a] *Institute of Sound and Vibration Research, University of Southampton, Southampton, SO17 1BJ, UK*
[b] *Aerodynamic and Flight Mechanics Research Group, University of Southampton, SO17 1BJ, UK*
[c] *Arup Acoustics, 8 St Thomas St, Winchester, SO23 9HE, UK*

Abstract

This paper presents an investigation, using both numerical and experimental methods, of the application of spanwise waviness to reduce aerodynamic noise from square bars. The numerical simulations are performed using the Delayed Detached-Eddy Simulation approach to obtain the near-field unsteady flow properties, which are then used to calculate the equivalent source terms in the Ffowcs Williams-Hawkings equation for far-field noise prediction. For a straight square bar in cross-flow, which produces strong tonal noise associated with the vortex shedding, a benchmark study showed good agreement between numerical simulations and measurements in terms of far-field noise spectra. Waviness is then introduced along the bar span and the influence of the amplitude and wavelength of the waviness is studied. When the wave amplitude is nearly half the bar width, a large noise reduction of as much as 30 dB is found from both numerical simulations and measurements, including a 10 dB reduction in the broadband level. The influence of the wavelength is much smaller. Analysis of the flow features showed that, with increased wave amplitudes, the spanwise flow becomes significant and strong crossflow vortices develop in the near wake which effectively suppress the primary vortex shedding. This reduces the noise level significantly, especially the tonal noise associated with the vortex shedding.

Keywords:
aerodynamic noise reduction, square bars, spanwise waviness, pantograph, vortex shedding

1. Introduction

Flow around bluff bodies, such as circular cylinders and rectangular or square bars, is of great practical importance in many industrial applications and environmental situations, e.g. structural design, flow-induced vibration, and flow-induced noise. The aerodynamic noise emission from bluff bodies has been an important research topic with many practical applications including components of aircraft landing gear [1] and high speed train pantographs [2]. Most research on the fundamentals of aerodynamic noise, its prediction and reduction have been carried out for circular cylinders. Structures with rectangular or square cross-sections are also common in these applications including, for example, the contact strip of a pantograph. The aim of the present study is to investigate the mechanisms of aerodynamic noise from square bars, and measures for noise reduction.

Measurements have been conducted on the aerodynamic noise radiated from square bars although not as extensively as for circular cylinders. King and Barsikow [3] measured and compared the acoustic properties of square, circular and elliptical cylinders. The effects of the incoming flow speed and bar aspect ratio (L/D, where L is the cylinder spanwise length and D is the width of the cross-section) were also assessed in the measurements. It was found that the noise level at the spectral peak, which is associated with the vortex shedding phenomenon, is $5-7$ dB higher for the square bar than for a circular cylinder. The effect of the aspect ratio on the vortex shedding frequency, measured by the non-dimensional Strouhal number ($St = fD/U_\infty$, where f is the vortex shedding frequency and U_∞

*Corresponding author. Tel.:+44 7701019401
Email address: xwone.liu@gmail.com (X. W. Liu)

is the freestream velocity) is smaller for square bars than for circular cylinders. The sound pressure level of radiated noise from cylinders at low Mach numbers generally follows a speed dependence of U_∞^6, which is a typical characteristic for noise dominated by surface pressure fluctuations. These findings have been confirmed by Latorre Iglesias et al. [4] who extended the available experimental database to higher Reynolds number ($Re = U_\infty D/\nu$, where ν is the kinematic viscosity) and yaw angles (the angle between the cylinder axis and the normal to the freestream velocity). The influence of the angle of attack for the square bar was also investigated.

To give a physical interpretation of the noise radiation, a good understanding of the near-field aerodynamic phenomena is necessary. The near-field flow features, such as the surface pressure fluctuations, the correlation of flow structures, the vortex formation and the turbulence transport in the wake for a square bar in cross-flow have been studied both experimentally [5, 6, 7, 8] and numerically [9, 10, 11], leading to improved understanding of noise generated by turbulent flow.

The noise generated by cylinders is dominated by a distinct peak in the spectrum at the vortex shedding frequency. The level of the spectral peak is directly related to the magnitude of the surface pressure fluctuations which are mainly caused by coherent periodic vortex shedding. It is therefore expected that the noise level can be reduced by suppressing the vortex shedding. Major achievements in passive flow control for suppressing the vortex shedding from bluff bodies were reviewed by Choi [12] who classified the methods as boundary-layer control and direct-wake control. Boundary-layer control is achieved through triggering the transition from laminar to turbulent flow before flow separation, for example by introducing surface roughness. This method makes use of the so-called drag crisis which is a typical characteristic for circular cylinder flow at critical Reynolds numbers, and reduces the induced drag significantly through delay of flow separation.

For direct-wake control, the purpose is to introduce two-dimensional (2-D) or three-dimensional (3-D) disturbances to disrupt the interaction between the upper and lower separated shear layers and hence suppress the vortex shedding. Among many others, Roshko [13] installed a splitter plate behind the cylinder, which was found to be effective in stabilizing the near wake by delaying the shear-layer interaction. This results in a lengthened vortex formation and hence increases in the base pressure which results in a drag reduction. However, this method requires a relatively long splitter plate (length about $3D$) for effective drag reduction, which may not be practical in many situations.

The method of generating 3-D disturbances has also been investigated. Bearman and Owen [14] measured the drag reduction for a rectangular bar at $Re = 4 \times 10^4$ due to the introduction of a spanwise waviness on the front stagnation face. The wavelength and amplitude of the waviness were found to be important in reducing drag and suppressing vortex shedding. In addition, spanwise waviness was also introduced on the rear surface, however with little effect on drag reduction. Darekar and Sherwin [15] confirmed the effect of spanwise waviness on the drag reduction by carrying out numerical simulations for a square bar with spanwise waviness on both front and rear faces, primarily at $Re = 100$ where separated flow from the sharp leading edge reattaches on the upper and lower surfaces for a straight square bar. Three different flow patterns were found when the waviness amplitude was increased from 0 to $0.25D$. The near-wake region was found to become fully stable with the lift fluctuations reduced nearly to zero for high amplitudes of the waviness. It was argued that the suppression of the vortex shedding can be attributed to the redistribution of vorticity; the spanwise vorticity component is re-distributed into streamwise and crossflow vorticity components, which delays the interaction of the shear layer in the near-base region. They also indicated that the 3-D effects are introduced earlier for the case with waviness on the front stagnation face than on the rear face. Lam and Lin [16] extended the concept of waviness to a circular cylinder at $Re = 100$ by introducing a sinusoidal variation of the cross-section along the spanwise direction, and found significant reductions in the mean and fluctuating force coefficients. This was attributed to variation in the separation line along the span which leads to the distortion of the 2-D shear layer structures into three dimensions. Other methods, such as attaching hemispherical bumps in a spiral arrangement on the cylinder surface [18] or mounting small tabs on the trailing edges [17], have been found to introduce similar 3-D effects.

The investigations mentioned above primarily focussed on the reduction of the forces acting on bluff bodies with emphasis on flow-induced vibration. For reducing the noise emissions, Ikeda [19] tested three different measures in an open-jet wind tunnel which were intended to reduce noise from circular cylinders. The cases tested were a cylinder with a spiral wire, a cylinder with discrete holes and a cylinder with a continuous slot; these all showed effective suppression of the vortex shedding as well as noise reduction. However, the slot generated a new tonal noise at a higher frequency. The case with holes was found to be the most effective, but it was emphasized that the hole sizes need to be determined carefully to separate the hole resonance frequency from the cylinder vortex shedding frequency.

Takaishi et al. [20] carried out numerical simulations for a circular cylinder with holes and found that dipole sound sources were mainly suppressed due to the momentum injected through the holes. King and Pfizenmaier [3] tested two measures to reduce noise from circular cylinders; one is to attach a rectangular rib on the back of the cylinder and the other is to introduce roughness on the cylinder surface. Both methods were found to reduce the noise level, especially the tonal noise. Sueki et al. [21] applied porous materials to cylinders and found good performance in reducing the tonal noise as well as the broadband noise.

Relevant work can also be found in the applications to jet engine and aerofoil noise reduction. Ver [22] proposed sawtooth serrations to reduce the exhaust noise of jet engines. Chevrons are now commonly seen in jet engines. Hersh et al. [23], Arndt and Nagel [24], and Longhouse [25] attached a serrated strip near the leading edge of an aerofoil to reduce the correlation length, leading to noise reduction. Hersh and Hayden [26] found tonal noise reductions at small angle of attack and broadband noise reductions for stalled aerofoils when a wavy leading edge is applied. More recently, Hansen et al. [27] investigated the flow characteristics for a NACA 0021 aerofoil with leading edge serrations through both numerical simulations and experiments. They found that the presence of strong pressure gradients near the leading edge gives rise to the stretch and diffusion of the vorticity in a highly 3-D manner, which leads to the generation of streamwise vortices. The modified aerofoils showed slightly improved performance in terms of their lift and drag coefficients. The 3-D evolution of the streamwise vortices was further studied by Pérez-Torró and Kim [28] using Large Eddy Simulation (LES). Kim et al. [29] studied the effect of leading edge serrations on reducing the noise generated by a flat-plate aerofoil interacting with the impinging turbulence by solving the Euler equations. It was found that the source strength diminished rapidly around the hill region (at the middle between the peak and the valley of the waviness) due to geometric obliqueness which leads to reduced sound pressure levels. They also identified a phase interference effect that is particularly significant between the peak and the hill which contributes to the noise reduction in the mid- to high-frequency range. Chaitanya et al. [30] derived a simple scaling law to predict the noise reduction for arbitrary serration amplitude and wavelength on an aerofoil and obtained an optimum wavelength at which the maximum sound power reduction is achieved. Turner and Kim [31] explored the relationships between the vortex-induced velocity perturbation and the wall pressure fluctuation on the wavy leading edge geometry. More work by using wavy leading/trailing edges on reducing aerodynamic noise from aerofoils can be found in Lau et al. [32] and Clair et al. [33].

In the present study, spanwise waviness is introduced to both the front and rear faces of a square bar to investigate the potential for noise reduction both numerically and experimentally. In Section 2 the numerical methodology used in this work, which is based on the Delayed Detached Eddy Simulation approach, is introduced briefly. The computational set-up and results for a straight square bar are presented in Section 3 which includes a study of the influence of the spanwise grid resolution and Reynolds number. Section 4 is for the wavy square bar and includes the computational set-up and the numerical results focusing on the influence of the wavelength and the wave amplitude. Measurements on straight and wavy bars are described in Section 5. This includes the experimental set-up and the validation of the numerical results for far-field noise spectra. The effects of the wave amplitude and wavelength on the far-field noise and the flow physics associated with noise reduction mechanisms are analysed from the simulations in Section 6. Conclusions are given in Section 7.

2. Numerical methodology

All aeroacoustic characteristics, including the aerodynamic sound generation and propagation, can in principle be described by the full compressible Navier-Stokes equations, which are, however, very difficult to solve due to the non-linearity of the partial differential equations. Computational aeroacoustic techniques can be classified into two main categories: direct and hybrid approaches [34]. The direct method aims to obtain acoustic results directly from the Navier-Stokes equation, therefore introducing extremely high computational cost which is not practical for most industrial applications. Therefore, in the current study, a two-step hybrid method is used which is computationally more efficient. In contrast to direct methods, hybrid methods do not aim to capture the radiated sound field but to resolve only the sound-generating near-field through the Navier-Stokes equations. The noise radiated to the far-field is obtained by using an acoustic analogy based on the equivalent noise sources obtained from the unsteady flow field determined using computational fluid dynamics (CFD) techniques. Hybrid approaches have been successfully used for the prediction of aerodynamic noise from components of aircraft landing gear [1] and high speed train pantographs [35].

The Reynolds-average Navier-Stokes (RANS) model, as one of the CFD methods, is widely adopted for practical engineering applications due to its low computational cost. However, RANS approaches were developed to provide time-averaged data, and therefore are not suitable for acoustic problems due to the unsteady nature of the acoustic field. Unsteady RANS can capture slowly varying unsteady flow structures but cannot resolve all unsteady scales, which are responsible for acoustic radiation. The LES model has the capability of resolving large energy-containing eddies but it is not practicable in most industrial applications due to its high computational cost. Therefore, hybrid RANS-LES methods were developed to benefit from the merits of both techniques. These have specific advantages in resolving wall-bounded flows, where the entire boundary layer is treated by URANS models to save computational cost and the LES treatment is applied to the separated flow regions further away from the walls to resolve the large scale unsteadiness. The most common hybrid RANS-LES method is detached eddy simulation (DES) which was first proposed by Spalart, who applied the Spalart-Allmaras (S-A) model for the RANS region [36]. The standard DES method has a significant dependency on the grid spacing which can cause early switch from RANS to LES inside the boundary layer, and can lead to unphysical flow phenomena, such as grid-induced separation [37]. To avoid this limitation, delayed detached-eddy simulation (DDES) was proposed by Spalart [38] who applied a modification to the original DES length scale to ensure the attached boundary layer is solved in RANS mode independently of the grid resolution.

The acoustic analogy employed within the current work is that of Ffowcs Williams and Hawkings [39], who extended the analogies of Lighthill [40] and Curle [41] to consider the presence of a surface in arbitrary motion. The Ffowcs Williams and Hawkings (FW-H) equation is represented as,

$$\left(\frac{\partial^2}{\partial t^2} - c_0^2\nabla^2\right)\Big(H(f)\rho'\Big) = \frac{\partial^2}{\partial x_i \partial x_j}\Big(T_{ij}H(f)\Big) - \frac{\partial}{\partial x_i}\Big(F_i\delta(f)\Big) + \frac{\partial}{\partial t}\Big(Q\delta(f)\Big) \tag{1}$$

where $\delta(f)$ is the Dirac delta function, and $H(f)$ is the Heaviside function. $f = 0$ defines the surface, which may be in arbitrary motion, over which integration is performed for the surface sources. $H(f) = 0$ inside the integral surface ($f < 0$) and $H(f) = 1$ elsewhere ($f \geq 0$). $\rho' = \rho - \rho_0$ is the density fluctuation, and c_0 is the sound speed for the undisturbed medium. The first term on the right-hand side of Equation (1), with $T_{ij} = \rho u_i u_j + (p - c_0^2\rho') - \tau_{ij}$, is the quadrupole source term which normally results from non-linear aerodynamic phenomena such as non-linear wave propagation, shocks, vorticity and turbulence in the flow field. Here, u_i is the flow velocity component in the direction x_i ($i = 1, 2, 3$). τ_{ij} is the viscous stress tensor. The second term, with $F_i = pn_i - \tau_{ij}n_j + \rho u_i(u_n - v_n)$, is the dipole source which is generated by the unsteady forces acting on the fluid due to the presence of the body. Here p is the pressure, $\mathbf{n}$ is the normal unit vector of the integral surface, u_n is the fluid velocity component normal to the integral surface, v_n is the normal velocity of the surface itself. The third term, $Q = \rho_0 v_n + \rho(u_n - v_n)$, is the monopole source which represents the noise generated by unsteady mass flux through the surface.

The current interest is in low subsonic flow ($M < 0.3$) which is typical for the application to high-speed trains and aircraft landing gear. In such cases the influence of compressibility is small, and the Navier-Stokes equations are therefore solved in incompressible form. The contribution of the quadrupole sources is not considered since it is much less significant compared with other contributions for these Mach numbers [42]. This allows the FW-H integral surface to be placed on the solid surface. Lockard et al. [1] compared predicted noise from circular cylinders by integrating the FW-H equations on solid and permeable surfaces, and found that there were only minor differences for a Mach number of 0.166. When the FW-H is evaluated over the solid surface and $v_n = 0$, the monopole term also vanishes. Therefore only the dipole source due to wall pressure fluctuations is considered.

3. Straight square bar

3.1. Computational set-up

The geometrical parameters and mesh topology used for the straight bar are shown in Figure 1. The $x-$direction is in the direction of the incoming flow, U_∞, the $y-$direction is perpendicular to the inflow and the $z-$direction is along the bar axis. The bar has a cross-section of $D = 0.041$ m (height) and $B = 0.0431$ m (width), which are determined according to the cross-section of the contact strips from a typical high-speed train pantograph. Since the width and the height are almost identical, the cross-section of the bar is considered as effectively a square. The Reynolds number $Re = U_\infty D/\nu$ is determined based on D, the inflow speed U_∞ and the kinematic viscosity ν.

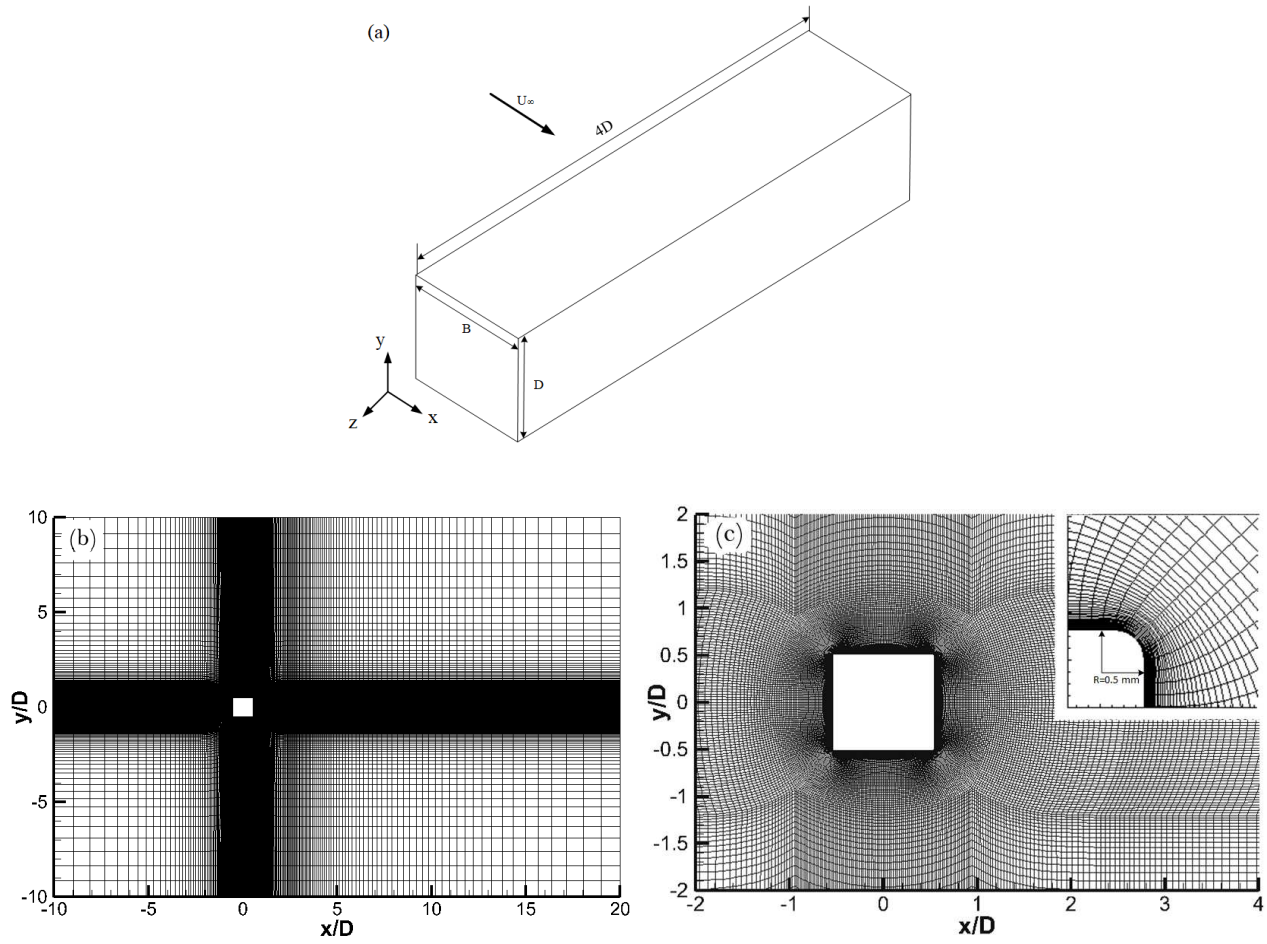

Figure 1: Computational set-up. (a) geometry definition, (b) grid configuration for whole domain, (c) grid in the vicinity of the bar.

In the $x-$direction, the computational domain extends over $L_x = 30D$ with the centre of the bar located at $10D$ from the upstream boundary. In the $y-$direction, the domain width is $L_y = 20D$ with an equal distance of $10D$ from the bar centre to the top and bottom boundaries. The effect of the domain size in the $x-y$ plane has been studied by Sohankar et al. [10] who found that a computational domain with $L_x = 24D$ and $L_y = 16D$ is sufficient to get reasonable results. Trias et al. [11] investigated the spanwise two-point correlation in the wake of the bar for $Re = 2.2 \times 10^4$ and found that the correlation values fall to zero at a separation distance less than $L_z = 2D$. This suggests that a domain size of $4D$ is sufficient to allow periodic boundary conditions to be applied. In this study, a length of $L_z = 4D$ was chosen in the spanwise direction, which has been used in most previous numerical studies [9][10][11].

In this work, the S-A turbulence model is adopted in DDES to solve the boundary layer region, which requires a very fine near-wall spacing, with $y_1^+ \leq 1$. $y_1^+ = u_\tau y_1/\nu$ is the non-dimensional wall distance (u_τ is the friction velocity at the nearest wall, ν is the kinematic viscosity of the fluid and y_1 is the height of the first layer cell adjacent to the bar surface). Based on the predefined requirement ($y_1^+ \leq 1$), a suitable value for y_1 can be estimated. The actual y_1^+ distribution around the bar surface was checked after completion of the simulation and is shown in Figure 2. It can be seen that the overall values of y_1^+ are lower than 1, which meets the requirement. The maximum value of y_1^+ appears at the front surface edges, A and B. To save the computational cost and improve the mesh quality near the bar corners, the sharp corners are rounded with a radius of 0.5 mm ($\approx 0.01D$), as shown in the zoom−in plot on the upper right of Figure 1(c). This alteration to the geometry is not expected to have any effect on the flow features, and also makes the geometry closer to the actual panhead.

The grids are non-uniform in the $x-y$ plane with a maximum growth ratio of 1.1 in the wake region and away from the wall. The mesh is denser near the corners and is coarsened close to the middle of each side, which gives a maximum width-to-height ratio $\Delta s/y_1 = 180$, appearing in the first layer cell at the middle of the bar surfaces. This maximum aspect ratio is considered adequate based on a previous grid sensitivity study of circular cylinder flow [35]. In the spanwise direction, a coarser grid resolution can be applied for a square bar compared to a circular cylinder since the flow separation is fixed at the front corners along the span whereas for a circular cylinder the separation can vary along the span and in time. Effects of grid resolution in the spanwise direction will be assessed in the next section.

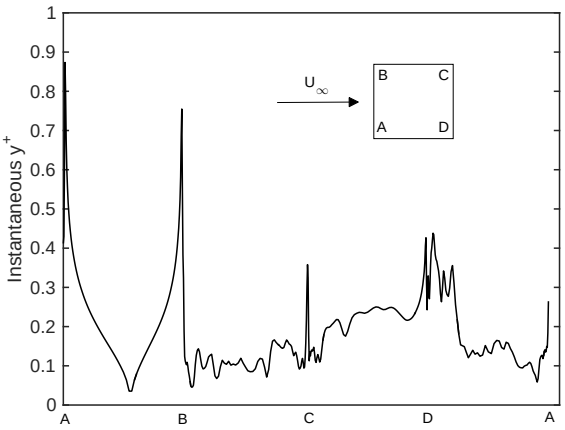

Figure 2: Instantaneous y_1^+ distribution around the bar surface.

The upstream boundary (at $x = -10D$) is defined as a velocity inlet and the downstream boundary is set to pressure outlet with zero gauge pressure. At the upper and lower boundaries, symmetry boundary conditions are applied. The solid surface of the bar is set as a non-slip wall. In the spanwise direction, periodic boundary conditions are imposed to model a bar with infinite span. Similar boundary conditions have been successfully used in previous works [9][10][11]. The flow simulations are carried out in OpenFOAM version 2.3.0. A second-order implicit scheme is applied for the temporal discretization, and a total variation diminishing scheme is used for the convection term. For the pressure-velocity coupling term, a PISO algorithm is used. After obtaining the surface pressure fluctuations, the aerodynamic noise is predicted using the FW-H equation in FLUENT.

3.2. Influence of the spanwise grid resolution

In this section, the influence of the spanwise grid resolution is investigated for the straight bar with a freestream velocity of $U_\infty = 30$ m/s, corresponding to $Re = U_\infty D/\nu = 8.2 \times 10^4$. For this case, the 2-D mesh in the $x-y$ plane is built based on a previous grid sensitivity study for a circular cylinder [35] which is considered adequate as the flow over a bar with its fixed separation is no more complex than flow over a circular cylinder. Therefore only the spanwise grid resolution is investigated here. The number of cells in the $x-y$ plane is kept at 58,871. A summary of the cases is given in Table 1. The number of cells in the $z-$direction N_z is progressively increased from 32 to 82. The dimensionless time step ($\Delta t U_\infty/D$) is 0.0015, which corresponds to a physical time step of 2×10^{-6} s, ensuring that the maximum Courant-Friedrichs-Lewy (CFL) number is less than 2 to give a stable temporal resolution with the implicit time marching scheme used [43]. The CFL number is defined as CFL $= \Delta t U_\infty/\Delta x$, where Δx is the smallest cell size in the streamwise direction.

Aerodynamic quantities, such as the mean drag coefficient C_D ($= \frac{F_{\text{drag}}}{0.5\rho U_\infty^2 DL}$, where F_{drag} is the drag force), the base pressure coefficient C_{pb} (the pressure coefficient is defined as $C_p = \frac{p-p_\infty}{0.5\rho U_\infty^2}$ with p being the pressure on the bar surface and p_∞ the reference pressure, C_{pb} is evaluated at the back of the bar), the root-mean-square (rms) lift coefficient $C_{L,\text{rms}}$ (the lift coefficient C_L is defined as $C_L = \frac{F_{\text{lift}}}{0.5\rho U_\infty^2 DL}$ with F_{lift} being the lift force), the rms drag coefficient $C_{D,\text{rms}}$

Table 1: Summary of the global flow parameters for straight bar at $Re = 8.2 \times 10^4$.

Cases	Re	Grid	C_D	$-C_{pb}$	$C_{L,\mathrm{rms}}$	$C_{D,\mathrm{rms}}$	St_p
$N_z = 32$	8.2×10^4	$58,871 \times 32$	2.21	1.45	1.51	0.28	0.129
$N_z = 54$	8.2×10^4	$58,871 \times 54$	2.08	1.35	1.38	0.21	0.129
$N_z = 82$	8.2×10^4	$58,871 \times 82$	2.05	1.34	1.32	0.18	0.129
Exp. Lyn et al. [8]	2.14×10^4		2.1	–	–	–	0.13
Exp. Norberg [44]	2.2×10^4		2.10	1.34	–	–	0.130
Exp. Vickery [5]	1×10^5		2.05	1.35	1.3	0.17	0.12
Exp. Lee [45]	1.76×10^5		2.04	1.33	1.19	0.22	0.122
LES. Sohankar et al. [10]	2.2×10^4	$185 \times 105 \times 49$	2.09	1.38	1.39	0.19	0.128

and the Strouhal number at the spectral peak St_p are given in Table 1. The convergence of all statistics has been confirmed by comparing the statistics calculated from different time periods. The final statistics are sampled over 480 non-dimensional time units ($t^* = tU_\infty/D$), which corresponds to 62 shedding cycles for a Strouhal number of 0.13. The experimental data from Lyn et al. [8], Norberg [44], Vickey [5] and Lee [45] and the LES results from Sohankar et al. [10] are also given in Table 1 for comparison. Although the experiments have been conducted at different Reynolds numbers, there is little variation between the results, confirming the fact that flow over square bars is not sensitive to Reynolds number for $Re \geq 1 \times 10^4$ [46][47]. The LES simulations of Sohankar et al. [10] used different subgrid scale models and only the results from the dynamic one-equation model that the paper claimed to be the best are included for comparison here.

It can be seen that when N_z is increased from 32 to 54, C_D, $C_{L,\mathrm{rms}}$ and $C_{D,\mathrm{rms}}$ all reduce. The changes in $C_{L,\mathrm{rms}}$ and $C_{D,\mathrm{rms}}$ are larger, which indicates that the rms values are more sensitive to the grid resolution. When N_z is further increased from 54 to 82, C_D, $-C_{pb}$, $C_{L,\mathrm{rms}}$ and $C_{D,\mathrm{rms}}$ all reduce slightly, but the changes are very small and can be considered negligible. The Strouhal number is found to be insensitive to the grid resolution. The results from $N_z = 54$ and 82 give excellent agreement with the experimental data and also the LES results.

Comparisons for the surface pressure and the wake statistics are presented in Figure 3, which includes the current simulation results from different grid resolutions and the results from available experiments [44] and LES simulations [10]. Figure 3(a) shows the distributions of the mean pressure coefficient around the bar surface. The mean streamwise velocity (Figure 3(b)), the rms streamwise velocity (Figure 3(c)) and the rms cross-flow velocity (Figure 3(d)) are plotted along the centreline in the bar wake.

From Figure 3(a), it can be seen that the results at the windward side (AB) are unaffected by changes in N_z. However, at the leeward side (CD), C_p increases by 7% when N_z changes from 32 to 54, but remains nearly unchanged when N_z is further increased to 82. The pressure at the back has a strong effect on the drag as a higher back pressure would lead to a lower drag. Both cases with $N_z = 54$ and 82 give good agreement with the experiment and the LES simulation. The small difference between the current simulations and the experiments at the lateral sides (BC and AD) near the rear corners C and D can be related to the formation of small counter-rotating vortices near the rear corner under the big recirculation zone.

The recirculation length, L_r, is defined as the distance from the back of the bar to the point at which the mean streamwise velocity U_x recovers from negative values to zero and stays positive thereafter. It can be obtained from the mean streamwise velocity profile in the wake given in Figure 3(b). Flow within the recirculation region strongly influences the mean and unsteady aerodynamic forces on the bar; therefore the values of C_D, $C_{L,\mathrm{rms}}$ and $C_{D,\mathrm{rms}}$ are very sensitive to flow within the recirculation region, and the recirculation length is a very important parameter. This length is found to be virtually unchanged when varying N_z, hence only small changes are found in C_D, $C_{L,\mathrm{rms}}$ and $C_{D,\mathrm{rms}}$. However, the minimum velocity and the velocity recovery after $x/D = 2$ are seen to be influenced by the grid resolution. The results from $N_z = 54$ and 82 show good agreement with the experimental and the LES results for $x/D \leq 2$. The LES simulation of Sohankar et al. [10] predicted a faster recovery between $x/D = 2$ and 3 than the experiment and the current simulations, but the recovered velocity further downstream is close to the current simulations and slightly larger than the experiment.

Figure 3(c) shows the streamwise rms velocity. Unlike the mean flow quantities, C_p and U_x, u_{rms} does not show good convergence with increasing N_z; its maximum value reduces by about 10% when N_z is increased from 54 to

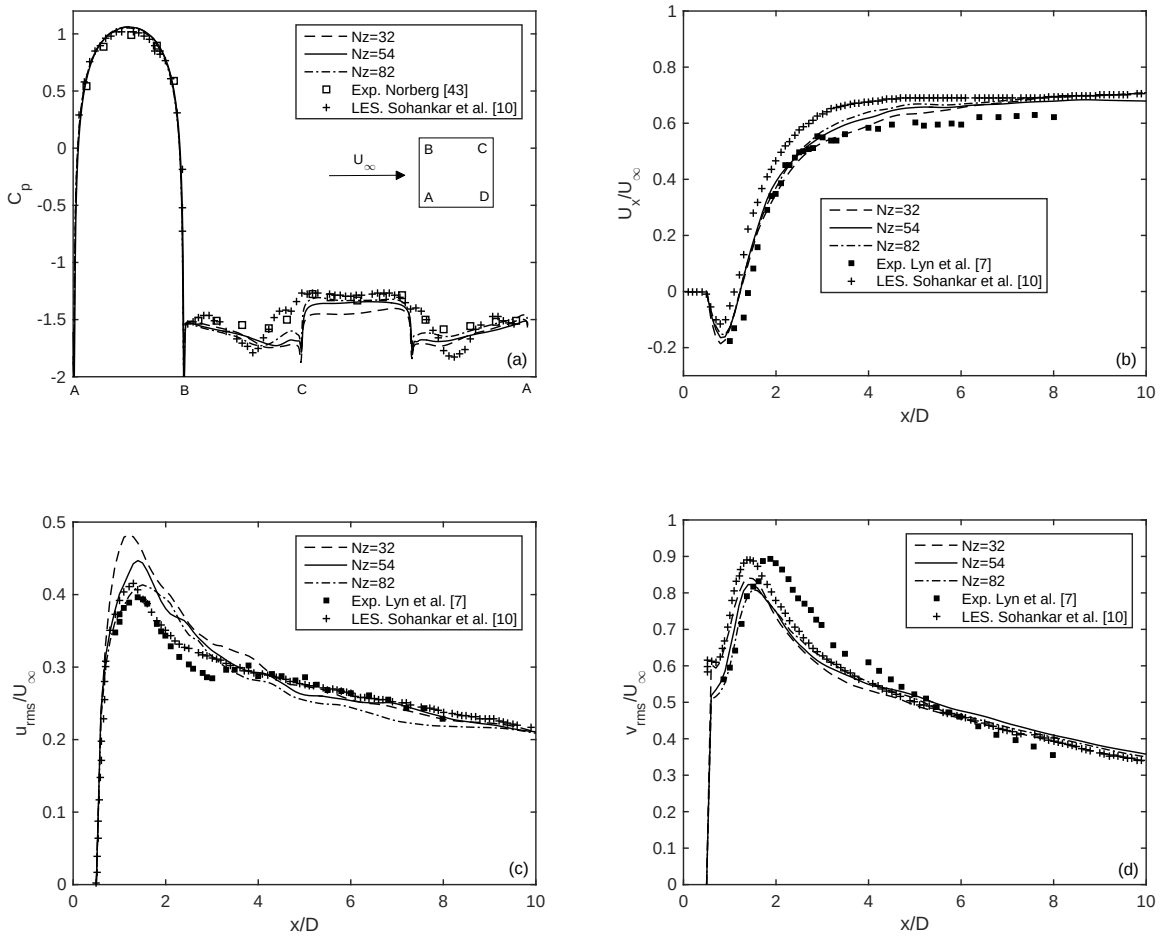

Figure 3: Comparison of mean surface quantities and wake statistics with existing experimental and LES results. (a) mean pressure coefficient along the bar surface. (b) mean streamwise velocity along the wake centreline. (c) RMS streamwise velocity along the wake centreline. (d) RMS cross-stream velocity along the wake centreline.

82, and there is a slight shift in the location of the peak. This indicates that the rms streamwise velocity is more sensitive to the grid resolution than the mean velocity. Current results obtained using $N_z = 82$ are much closer to the LES and experimental data, especially within the recirculation zone ($x/D < 1.75$) The influence of N_z on the rms cross-stream velocity v_{rms} shown in Figure 3(d) is much smaller than that on u_{rms}. The location of the maximum value of v_{rms} obtained from the current simulations is the same as in the LES results of Sohankar et al. [10], however both are closer to the bar than in the experiment, while the peak level is 8% lower. It may be noticed that this location corresponds to the end of the mean recirculation zone where $U_x = 0$ in Figure 3(b).

In general, the results are not sensitive to the spanwise grid resolution for square bars, since flow always separates at the leading edge and the transition occurs after the separation in the separated shear layer. The results for mean flow quantities and crossflow turbulence intensity reach convergence at $N_z = 54$ and give good agreement with both the experimental [8] and the LES [10] results, especially the statistics in the wake region which are often difficult to predict. Therefore $N_z = 54$ is used for the acoustic predictions. For other simulations with higher speeds, 60 and 110 m/s, the $x-y$ meshes are generated with the criteria which produces 2-D meshes with 83, 815 and 110, 352 grid points respectively, while $N_z = 96$ and 148 are employed respectively to maintain the same aspect ratio $\Delta z/\Delta y$ in the mesh. The good agreement seen with existing data also confirms that the mesh used in the $x - y$ plane is reasonable.

3.3. Influence of Reynolds number

In this section, results from different inflow speeds, 30, 60 and 110 m/s, are considered to study the effect of Reynolds number. The physical time step used in the simulations is 1×10^{-6} s for 60 m/s and 5×10^{-7} s for 110 m/s. A summary of results is presented in Table 2. It is found that C_D, $C_{L,\mathrm{rms}}$ and St vary only slightly with the Reynolds number, which indicates that the flow is not sensitive to the Reynolds number for the range of $Re = 8.2 \times 10^4 - 3.25 \times 10^5$ studied here. This is further confirmed through comparisons for mean surface pressure distributions and wake statistics, as shown in Figure 4. The flow structure is similar for different Reynolds numbers, hence only an example for $Re = 1.64 \times 10^5$ is shown in Figure 5.

Table 2: Summary of the global flow parameters for straight cylinders at different Reynolds numbers.

U_∞ [m/s]	Re	Grid	C_D	$-C_{pb}$	$C_{L,\mathrm{rms}}$	$C_{D,\mathrm{rms}}$	St
30	8.2×10^4	$58,871 \times 54$	2.08	1.35	1.38	0.21	0.129
60	1.64×10^5	$83,815 \times 96$	2.08	1.36	1.39	0.21	0.126
110	3.28×10^5	$110,352 \times 148$	2.08	1.35	1.41	0.25	0.132

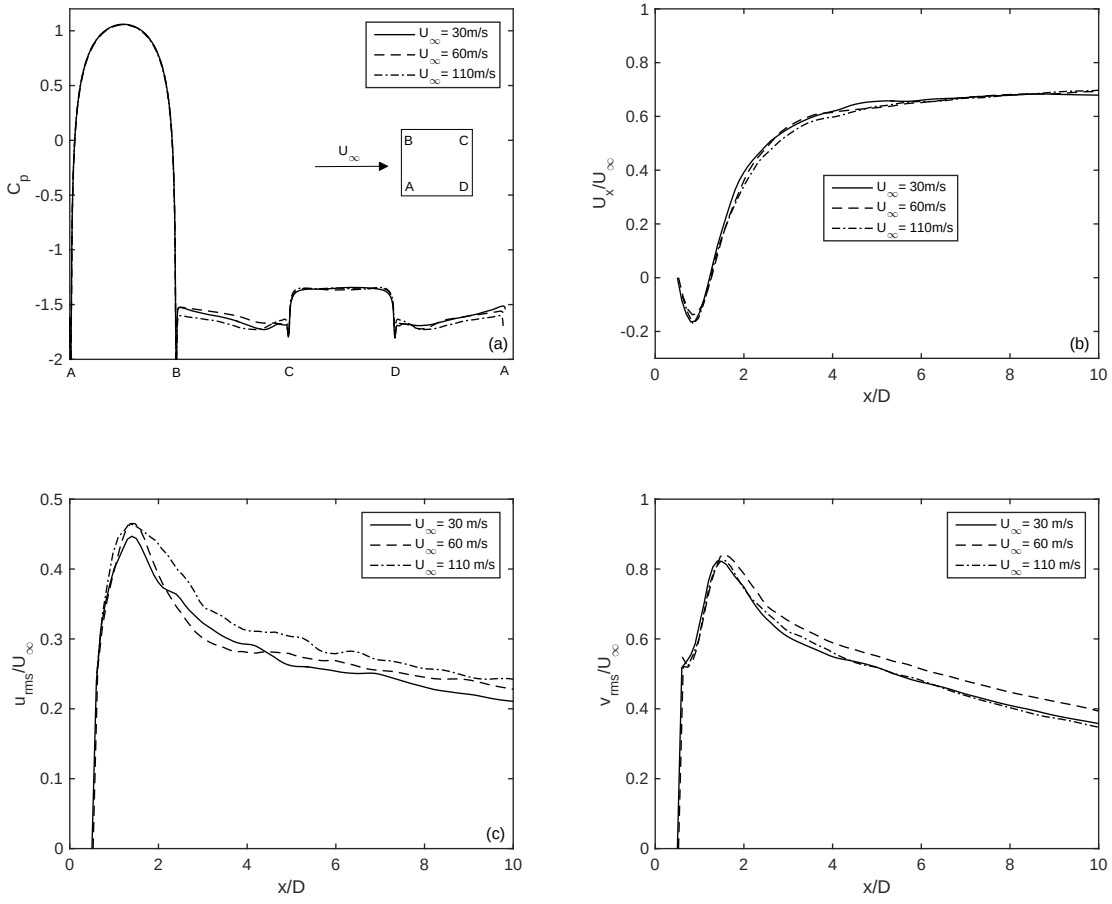

Figure 4: Comparison of mean surface quantities and wake statistics between different Reynolds numbers. (a) mean pressure coefficient along the bar surface. (b) mean streamwise velocity along the wake centreline. (c) RMS streamwise velocity along the wake centreline. (d) RMS cross-stream velocity along the wake centreline.

From Figure 4(a), it can be seen that the surface pressure distribution is consistent between different Reynolds numbers at the windward side (AB) and the leeside (CD). The nearly unchanged pressure at the leeside can be associated with a constant recirculation length for different Reynolds numbers, as can be seen in Figure 4(b). Unchanged back pressure C_{pb} leads to a constant value of C_D. The wake statistics, u_{rms} shown in Figure 4(c) and v_{rms} in Figure 4(d), which are normally very sensitive to Reynolds number, also show only small changes for these cases. Figure 5 shows that flow separation happens at the leading edge and the separated shear layer does not reattach to the lateral sides of the bar. In addition, Figure 5 shows two of small counter rotating vortices formed on the lateral sides near the front and rear corners (as detailed in inset) under the main separation, which are associated with the reattachment of the reverse flow in the wake. Changing the Reynolds number has little effect on the formation of these small vortices. Aeroacoustic features of the straight bar will be considered together with the wavy bar in the next chapter.

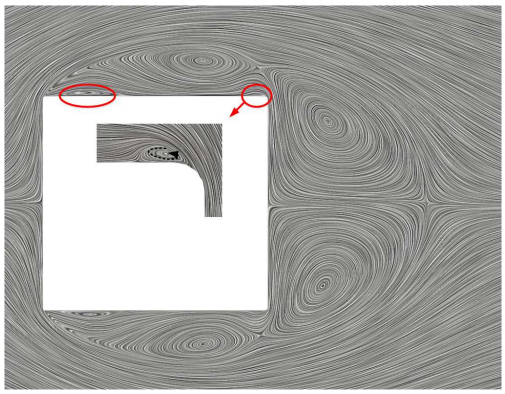

Figure 5: Mean streamlines in the $x-y$ plane for $Re = 8.2 \times 10^4$.

4. Wavy square bars

4.1. Computational set-up

Having established a suitable mesh for a straight bar, in this section different spanwise waviness is introduced to the bar. The geometry of the wavy bar is defined in Figure 6(a). The dimensions $D = 0.041$ m and $B = 0.0431$ m are the same as used for the straight case in Section 3. w is the wave peak-to-trough amplitude and λ is the wavelength. The cross-section furthest upstream is referred to as the 'peak', and that furtherest downstream as the 'valley' (see Figure 6(b)). In the present study, simulations are run for wavy bars at a freestream velocity of $U_\infty = 60$ m/s with different combinations of amplitudes and wavelengths, as listed in Table 3. The non-dimensional wavelength is chosen as $\lambda/D = 2$ or 4, and the non-dimensional amplitude w/D is gradually increased from 0.12 to 0.48 for each wavelength.

In Table 3, the domain sizes (L_x, L_y, L_z) in the $(x, y, z)-$directions, the number of cells in the $x-y$ plane and along the $z-$direction and the non-dimensional time step $\Delta t U_\infty/D$ are given. All wavy bar simulations employ the same domain size of $L_x = 30D$ and $L_y = 20D$ as used for straight cases in Section 3, which was also used by other researchers [15] for wavy bar simulations. The 3-D meshes are generated by extruding the 2-D mesh in the $x-y$ plane, which is the same as the straight case, along the wavy profile in the $z-$direction. Grids are uniformly distributed in the $z-$direction, as shown in Figure 6(b) for the surface mesh. The physical time step and the boundary conditions are the same as those used for the straight case. Although periodic boundary conditions are applied, the domain size in the spanwise direction also needs to be determined carefully to capture all significant spanwise flow features. In the current simulations, $L_z = 4D$ is again used for most cases, which includes two entire wavelengths for $\lambda = 2D$ and one wavelength for $\lambda = 4D$. In order to understand the influence of the number of waves along the span and for consistency with the cases of $\lambda = 2D$, a case with $L_z = 8D$ for $\lambda = 4D$ is also simulated.

Table 3: Geometrical and computational parameters for wavy bars

λ/D	w/D	$L_x \times L_y \times L_z$ $(/D)$	Grid	$\Delta t U_\infty/D$
2	0.12	$30 \times 20 \times 4$	$83,815 \times 96$	0.0015
2	0.24	$30 \times 20 \times 4$	$83,815 \times 96$	0.0015
2	0.36	$30 \times 20 \times 4$	$83,815 \times 96$	0.0015
2	0.48	$30 \times 20 \times 4$	$83,815 \times 96$	0.0015
4	0.12	$30 \times 20 \times 4$	$83,815 \times 96$	0.0015
4	0.24	$30 \times 20 \times 4$	$83,815 \times 96$	0.0015
4	0.36	$30 \times 20 \times 4$	$83,815 \times 96$	0.0015
4	0.48	$30 \times 20 \times 4$	$83,815 \times 96$	0.0015
4	0.24	$30 \times 20 \times 8$	$83,815 \times 192$	0.0015

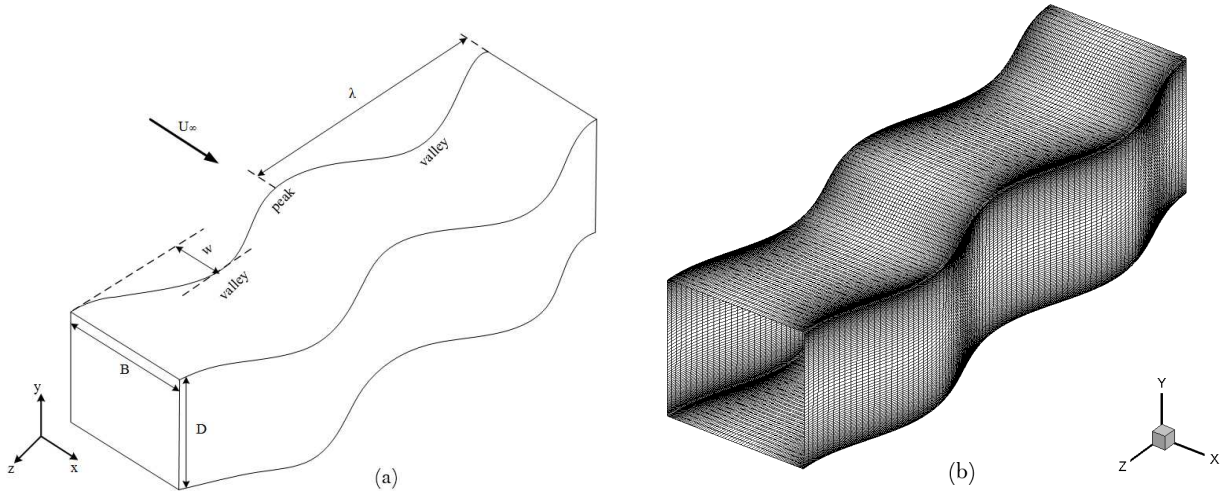

Figure 6: Definition of wavy bar geometry (a) and mesh configuration on the bar surface (b).

4.2. Aerodynamic results

The statistical and acoustic results discussed below are sampled over a time period from 0.28 to 0.58 s (this varies slightly between different cases) which corresponds to 55 shedding cycles for a Strouhal number of 0.13. The development of the flow to a statistically steady state prior to collecting statistics has been checked by comparing C_D, $C_{L,rms}$ and $C_{D,rms}$ calculated from different time periods. The power spectral density (PSD) was calculated based on Welch's method using a Hanning window with an overlap of 50% following Hu et al. [48]. Three segments were employed resulting in a frequency resolution of 6.6 Hz, which corresponds to Strouhal number resolution of 0.005.

4.2.1. Influence of waviness amplitude

Figure 7 compares PSDs of the lift and drag coefficients between the straight bar and the four wavy cases with different waviness amplitudes for $\lambda = 4D$. It is seen that between the straight bar and the wavy case with $w/D = 0.12$, the lift spectra show little difference over a wide frequency range. When the wave amplitude is increased to $w/D = 0.24$, the peak frequency remains nearly unchanged but there is a slight decrease in the peak level. Further increasing the waviness to $w/D = 0.36$, the peak frequency is increased slightly by 5% while the peak level is reduced by a factor of 100 (20 dB). Considerable reductions are also found in the spectral levels over all frequencies. Further increasing w/D to 0.48, the peak becomes broadband with a further decrease in its level, while there is little change in the levels at other frequencies compared with $w/D = 0.36$. This can be explained by a much lengthened vortex

formation length, which will be shown in Section 6. The reduction in the unsteady forces acting on the square bar was achieved by suppressing the vortex shedding from two aspects; one is to weaken the spanwise correlation, which has been explored in [28, 29, 30, 31] for aerofoil cases with leading edge serration applied; the other is to delay the shear-layer interaction, and thus obtain a lengthened vortex formation [13]. The former will have an influence only on the amplitude of the peak, while the latter can affect the whole frequency range. These are consistent with the flow features that have been found from simulations and will be analysed later.

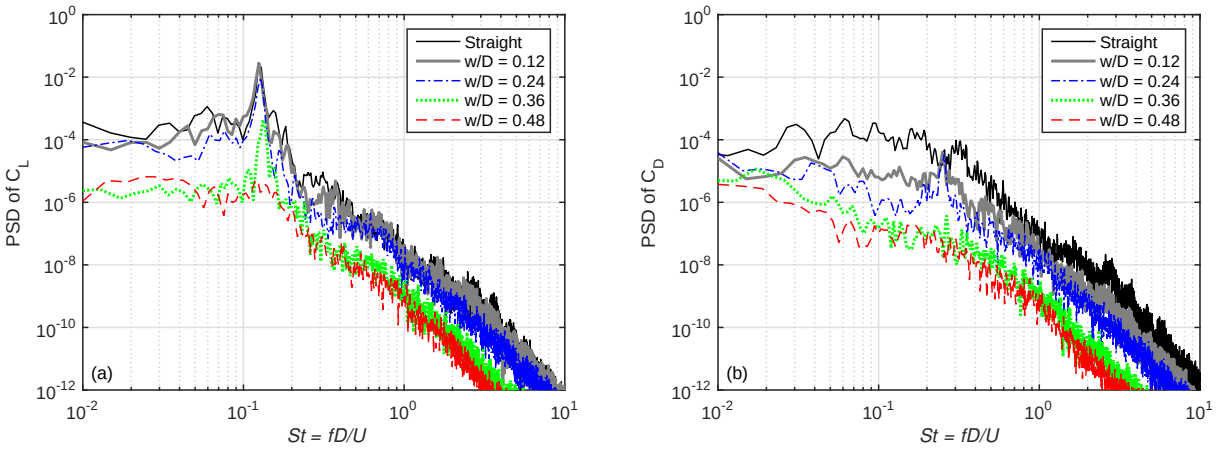

Figure 7: Comparisons of power spectral density of C_L (a) and C_D (b) between the straight bar and different wavy bars with $\lambda = 4D$.

The drag PSD levels are much smaller than the corresponding lift spectral levels for all the cases considered although the difference between them becomes smaller with increased wave amplitudes. For the straight case, the flow in the wake region is strongly 3-D, and no distinct peak is found in the drag spectrum. For $w/D = 0.12$ and 0.24, a weak peak is found at $St \approx 0.26$, while for $w/D = 0.36$ and 0.48, the spectra become broadband and have no distinguishable peak. Increasing the waviness amplitude, the overall levels of the drag PSD are noticeably reduced, particularly from $w/D = 0.24$ to 0.36.

It is known that the far-field radiated noise is closely related to the lift and drag fluctuations; hence it is expected that both the lift and drag dipoles will be significantly reduced for high wave amplitudes. The lift dipole will always be larger than the drag dipole but the difference between them will be smaller with increased wave amplitudes. Results for far-field noise will be given in Section 4.3 below. Changes of all flow quantities for span waviness with $\lambda = 2D$ are similar, therefore the results are not shown here.

4.2.2. Influence of wavelength and number of waves

Before comparing the results between different wavelengths, a comparison is given in Figure 8 of the PSDs of the lift and drag coefficients between different spanwise domain lengths, $L_z = 4D$ and $8D$, for $\lambda = 4D$ at $w/D = 0.24$. It can be seen that a very similar spectral shape is obtained for $L_z = 4D$ and $8D$. Both spectra are characterised by a distinct peak at the vortex shedding frequency ($St = 0.13$) in the lift spectrum, and at twice the vortex shedding frequency ($St = 0.26$) in the drag spectrum. Both the level and the frequency of the spectral peaks are nearly unchanged when the number of waves is increased from one to two by doubling the spanwise length. The levels at other frequencies are also similar for these two cases although the levels at low frequencies are slightly lower for $L_z = 4D$. To conclude, the effect caused by increasing the number of waves in the model is negligible especially for frequencies around the shedding peak and above, which allows comparisons between different wavelengths for a fixed spanwise length.

The results from $\lambda = 2D$, $L_z = 4D$ are also given in Figure 8 for comparison with $\lambda = 4D$ to assess the effect of different wavelengths. The lift spectra again show little difference in either the peak frequency or the peak level when varying the wavelength, while in the drag spectrum, the peak frequency is slightly higher and the peak level is lower for $\lambda = 2D$. The levels at other frequencies are also similar for these two wavelengths. This indicates that varying the

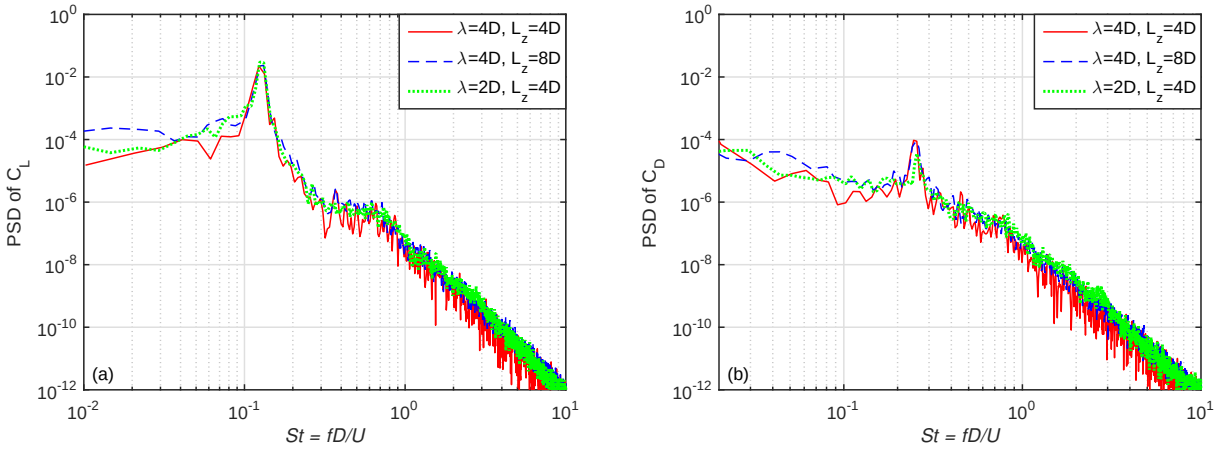

Figure 8: Comparisons of power spectral density of C_L (a) and C_D (b) between different spanwise domain lengths and different wavelengths at $w/D = 0.24$.

wavelength has negligible effect on the lift fluctuations, but a small effect on the drag fluctuations. These results differ from the LES simulations of Darekar and Sherwin [15] who studied different wavelengths from $\lambda = 1D$ to $10D$, and showed a strong dependency on the wavelength for square bars with spanwise waviness. However their cases were conducted at a low Reynolds number, $Re = 100$, at which the flow behaviour is predominantly 2-D for the straight bar and introducing the spanwise waviness leads to the transition to different 3-D modes. The spanwise flow structures in different 3-D modes are significantly affected by the wavelength of the waviness, which leads to the changes in the forces acting on the bar and the shedding frequency when varying the wavelength.

Figure 9 shows contour plots of the normalized turbulent kinetic energy (TKE) ($= \frac{1}{2}(u^2_{rms} + v^2_{rms} + w^2_{rms})/U^2_\infty$) in the spanwise $x - y$ planes at the waviness peak and valley for $w/D = 0.24$. Only half of each plane is presented due to its symmetry about the centreline. Figures 9(a,c) present comparisons between different spanwise domain lengths, $L_z = 4D$ and $8D$, with the wavelength fixed to $\lambda = 4D$, while Figures 9(b,d) compare cases with different numbers of waves, the spanwise domain length is fixed to $L_z = 4D$, and the wavelength is varied from $\lambda = 2D$ to $4D$.

Similar distributions of the wake TKE are found for different number of waves in the spanwise direction at both the peak (Figure 9(a)) and the valley (Figure 9(c)) cross-sections. The maximum TKE at the peak is located around the centreline, and appears at about $1D$ downstream of the bar. It moves only slightly closer to the bar when the span is doubled. The maximum TKE at the valley is much weaker, and high TKE values scatter and tend to appear away from the centreline, which is consistent between $L_z = 4D$ and $8D$. These results confirm the findings from the lift and drag spectra shown in Figure 8, that the spanwise domain length has little influence on the results.

From Figures 9(b,d), it is found that varying the wavelength leads to notable changes in the wake TKE distribution. On the peak plane, the maximum TKE occurs only slightly further downstream for $\lambda = 2D$ compared with $\lambda = 4D$ and the area of the maximum TKE is smaller at this wavelength. This indicates that the turbulence in the wake for $\lambda = 2D$ is weaker, which is consistent with the fact that weaker drag fluctuations are found for this wavelength, as shown in Figure 8(b). At the valley, the maximum TKE is found to be more concentrated around the centreline for $\lambda = 2D$, while it tends to be away from the centreline for $\lambda = 4D$ although the levels for these two cases are similar.

The above discussion shows that increasing the number of waves in the model from one to two has little effect on both lift and drag fluctuations, hence the far-field noise level, which is directly related to the lift and drag fluctuations, is expected to be unaffected. However, varying the wavelength causes some variations in the drag fluctuation as the TKE distributions in the wake are changed for different wavelengths, but the influence on the lift fluctuation is much smaller.

To investigate further the effect of the wavelength at different wave amplitudes, comparisons of PSDs of lift and drag coefficients between $\lambda = 2D$ and $4D$ for $w/D = 0.12$ and 0.36 are given in Figure 10. Figures 10(a,b)

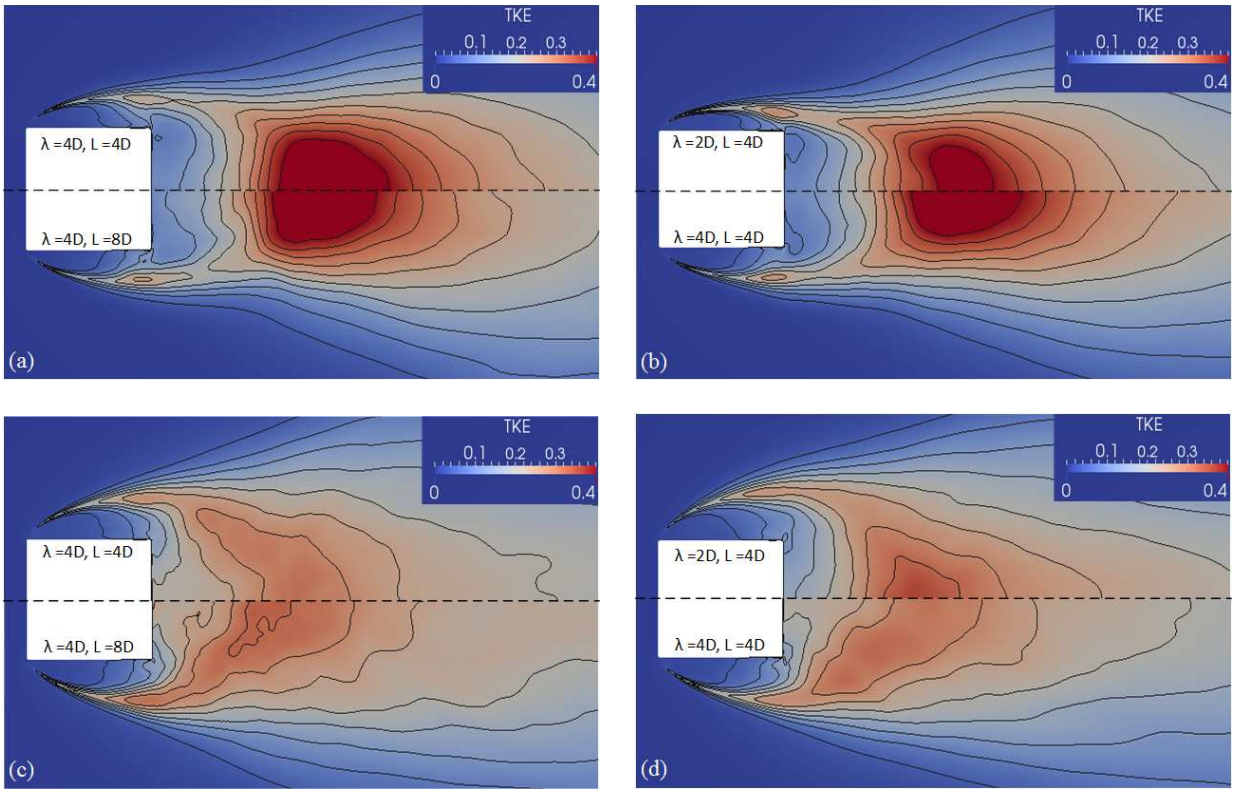

Figure 9: Normalized turbulent kinetic energy distributions (TKE) in the $x-y$ plane for different spanwise domain lengths (a,b) and wavelengths (c,d). (a,b) $w/D = 0.24$, peak. (c,d) $w/D = 0.24$, valley.

compare PSDs of lift coefficients for $w/D = 0.12$ and 0.36 respectively, and Figures 10(c,d) for drag coefficients. At $w/D = 0.12$, similar lift spectra are obtained for $\lambda = 2D$ and $4D$ although the peak level is slightly higher for $\lambda = 2D$. At $w/D = 0.36$, good agreement in terms of the peak frequency and the peak level is found between $\lambda = 2D$ and $4D$, but there is a broadband 'hump' between $St = 0.6$ and 1 for $\lambda = 2D$. This broadband 'hump' is also found in spectra at monitor points in the separated shear layer, indicating that it is associated with the shear layer instability. The clearer 'hump' occurring for $\lambda = 2D$ suggests that a more coherent secondary vortex is generated for this wavelength. Detailed analysis on vortex structures will be given later.

When comparing the drag spectra some differences are found between $\lambda = 2D$ and $4D$. At $w/D = 0.12$, a weak peak appears at $St \approx 0.26$ for $\lambda = 4D$, but it is difficult to identify this for $\lambda = 2D$. At $w/D = 0.36$, in addition to the differences in the peak, higher spectral levels at $St = 0.6 - 2$ are found for $\lambda = 2D$ which are similar to those found in the lift spectrum (Figure 10(b)). In general, varying the wavelength has little effect on the lift spectrum, but some effect on the drag spectrum for both $w/D = 0.12$ and 0.36.

4.2.3. A summary of aerodynamic parameters

The results of C_D, St_p, $C_{L,rms}$ and $C_{D,rms}$ are plotted against the wave amplitude w/D for all the simulated cases in Figure 11(a)-(d) respectively. It can be seen that the value of C_D is almost unchanged from the straight case to $w/D = 0.12$. As w/D is increased further, C_D begins to decrease gradually. The reduction in C_D is about 25% for $w/D = 0.48$ compared with the straight bar. In contrast, the peak Strouhal number St_p is not sensitive to the wave amplitude for $w/D \leq 0.36$ with only small variations. However, at $w/D = 0.48$, the peak for both $\lambda = 2D$ and $4D$ becomes broadband and a value of St_p cannot be identified. Only small differences are found in C_D and St_p between $\lambda = 2D$ and $4D$ cases with the same waviness amplitude.

Similar to C_D, $C_{L,rms}$ also shows little variation from the straight case to $w/D = 0.12$. However, for $w/D > 0.12$,

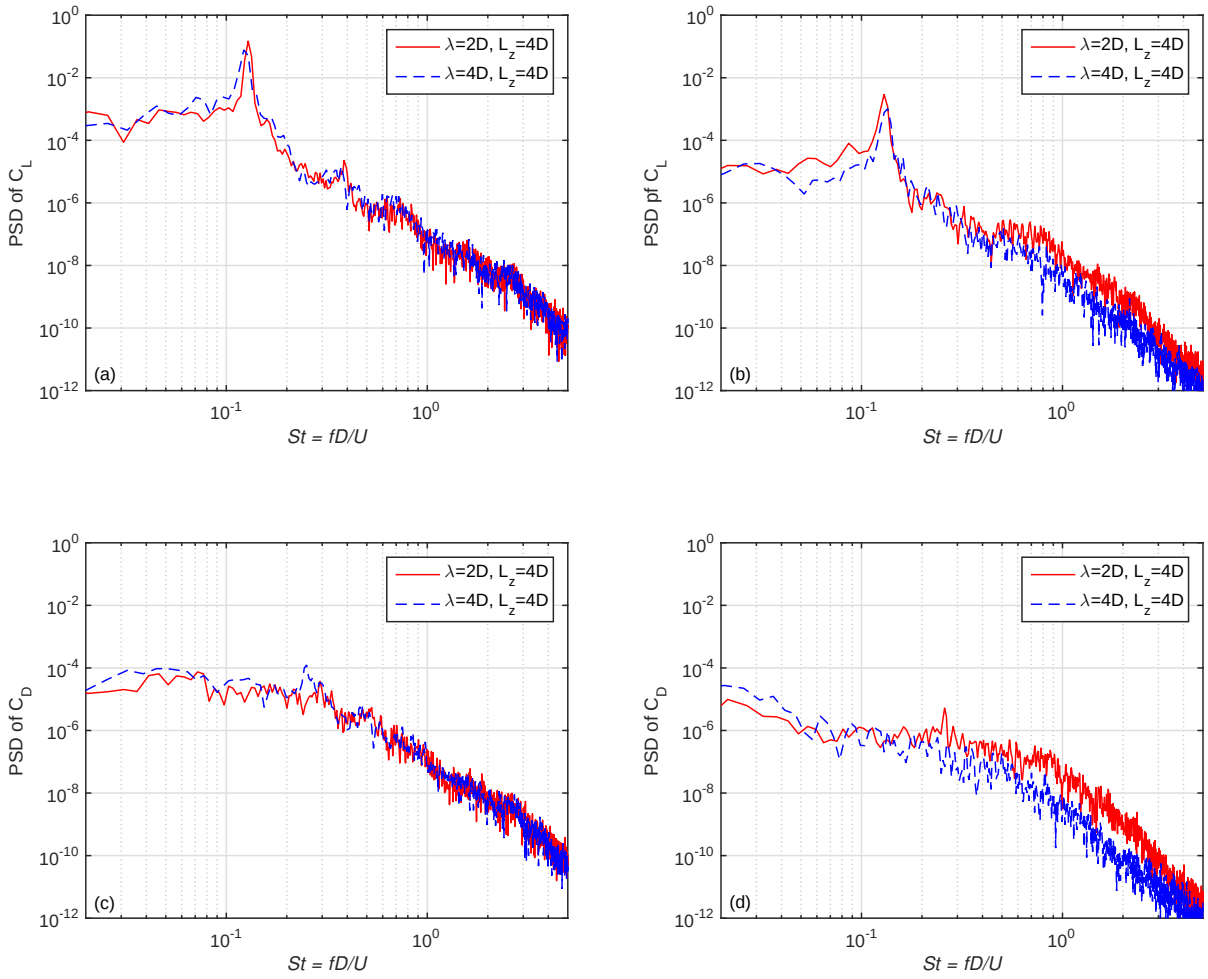

Figure 10: Comparisons of PSDs of C_L (a,b) and C_D (c,d) between $\lambda = 2D$ and $4D$ at different wave amplitudes. (a,c) $w/D = 0.12$. (b,d) $w/D = 0.36$.

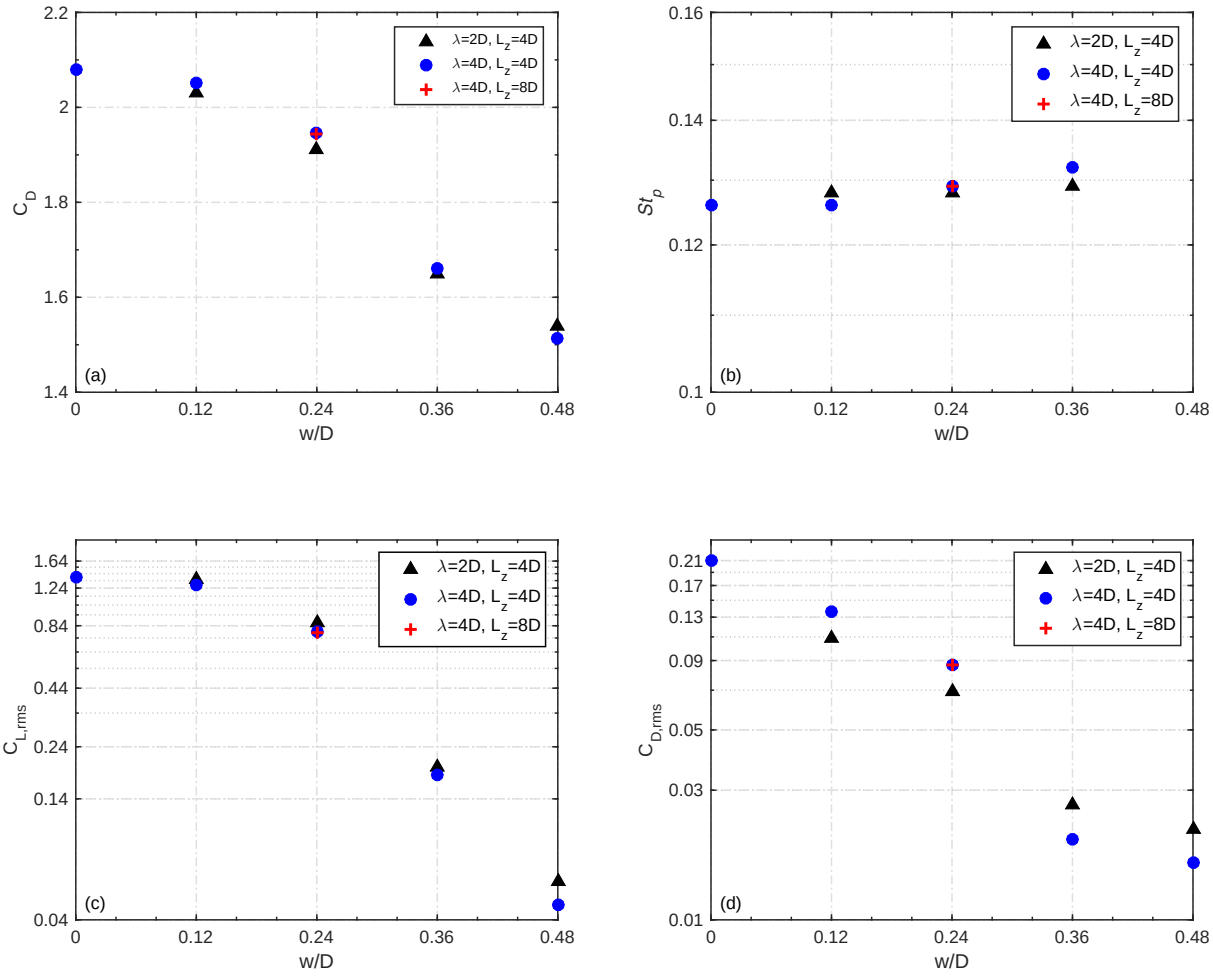

Figure 11: Variations of C_D (a), St_p (b), $C_{L,rms}$ (c) and $C_{D,rms}$ (d) with the wave amplitude.

the reduction in $C_{L,rms}$ is much larger. At $w/D = 0.24$, the reduction reaches 36%. A dramatic decrease of nearly 86% is found for $w/D = 0.36$ relative to the straight case. Further increasing w/D to 0.48, $C_{L,rms}$ is reduced by a factor of 30 to only 0.05. This trend is similar for different wavelengths, $\lambda = 2D$ and $4D$, although a small difference between them is found at $w/D = 0.48$.

$C_{D,rms}$ is always much smaller than $C_{L,rms}$. A notable decrease begins at $w/D = 0.12$, which occurs sooner than for C_D and $C_{L,rms}$. Significant decreases are also found at $w/D = 0.24$ and 0.36, but from 0.36 to 0.48, the decrease is much smaller, which is different from that found for $C_{L,rms}$. In addition, the differences in $C_{D,rms}$ between different wavelengths are more apparent than for C_D and $C_{L,rms}$, and these differences become more significant with increased wave amplitudes. In each plot, the results from the case of $\lambda = 4D$ and $L_z = 8D$ are also given at $w/D = 0.24$. Little variation is found in all the parameters between different spanwise domain lengths for $\lambda = 4D$. The above discussions suggest that the wave amplitude makes the main contribution to the variations in C_D, $C_{L,rms}$ and $C_{D,rms}$ and the effect of wavelength appears to be important only for $C_{D,rms}$ at high wave amplitudes.

4.3. Aeroacoustic results

Time histories of flow solutions obtained from CFD are fed to a FW-H solver for far-field noise prediction, with the integration surface placed on the cylinder. No periodic boundary condition is applied for the acoustic calculation, and only the actual length of the model, 4D, is taken into account for the spanwise direction. The far-field receivers are located on two planes with radius $R = 5$ m ($122D$) parallel to the incoming flow. One is normal to the bar axis ($x - y$ plane), as seen in Figure 12(a), and the other is parallel to the bar axis ($x - z$ plane), as shown in Figure 12(b). In each plane 72 receivers are located at 5° intervals.

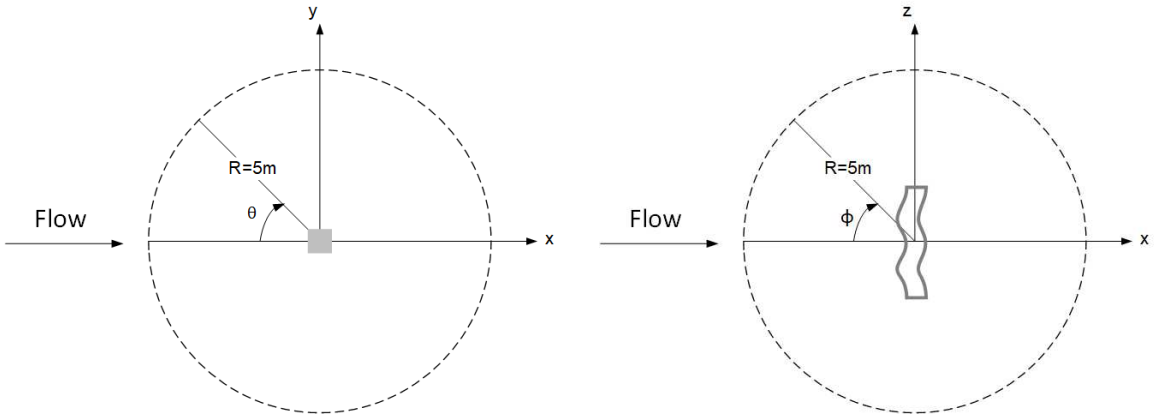

Figure 12: The locations of the far-field receivers in the simulations. (a) $x - y$ plane, normal to the bar axis. (b) $x - z$ plane, parallel to the bar axis.

Figure 13 shows the far-field narrow-band PSD of sound pressure for $\lambda = 4D$ at selected receivers. Figure 13(a) is for the receiver in the $x - y$ plane above the bar ($\theta = 90°$) which is mainly influenced by the lift fluctuations, Figure 13(b) is for the receiver downstream of the bar ($\theta = 180°$) where the drag dipole dominates, and Figure 13(c) is for the receiver in the spanwise direction (in $x - z$ plane $\phi = 90°$) to assess the radiation in the spanwise direction. Figure 13(a) shows that for both the straight and wavy cases, the noise level at the receiver above the bar is much higher than at the other two receivers. Compared with the straight bar, there is little change in the frequency and the level of the noise spectral peak at $\theta = 90°$ for $w/D = 0.12$ and 0.24. When the amplitude is increased to $w/D = 0.36$, the peak frequency is nearly unchanged but the peak level is reduced by 20 dB. In addition, considerable reductions in the levels are also found at other frequencies. Increasing the waviness further from $w/D = 0.36$ to 0.48, the spectral peak becomes broadband and its level is reduced by a further 15 dB, while the levels at other frequencies show little difference. These results are consistent with the lift coefficients in Figure 7(a).

The noise spectra in the drag direction (Figure 13(b)) display a broad peak at $St_p \approx 0.26$ for $w/D = 0.12$ and 0.24, whereas the spectra become broadband for $w/D = 0.36$ and 0.48. Successive reductions are found in the overall noise levels with increased wave amplitudes, which are more significant from $w/D = 0.24$ to 0.36. However, from $w/D = 0.36$ to 0.48, the overall levels are nearly unchanged. These results are consistent with the PSDs of drag coefficient shown in Figure 7(b). Figure 13(c) shows that the noise levels for the receiver in the spanwise direction are several orders of magnitude smaller than the tonal peak level for the receiver above the bar. Changing the wave amplitude only has slight effect on the spectral levels at high frequencies.

The tonal peak level at $\theta = 90°$ and the overall sound pressure level (OASPL) at $\theta = 90°$, 180° and $\phi = 90°$ for the straight and wavy cases are listed in Table 4 and plotted in Figure 14. The OASPL is obtained by integrating the PSD over the frequency range corresponding to $St = 0.02 - 2$. It can be seen that for both the straight and wavy cases, the OASPL is always about $11 - 14$ dB higher than the tonal peak level except for $w/D = 0.48$ at which the tonal peak is difficult to identify. There is only a slight difference, $1 - 2$ dB, between $\lambda = 2D$ and $4D$ for both the tonal peak level and the OASPL.

The far-field noise directivities in the $x - y$ and $x - z$ plane are presented in Figure 15. In the $x - y$ plane, the directivity pattern is dominated by the lift dipole with the maximum levels occurring in the lift direction, $\theta = 90°$ and 270°. Similar OASPLs, within 1 dB, are found for $\lambda = 2D$ and $4D$ at $w/D \leq 0.24$, while at $w/D = 0.36$, the minimum

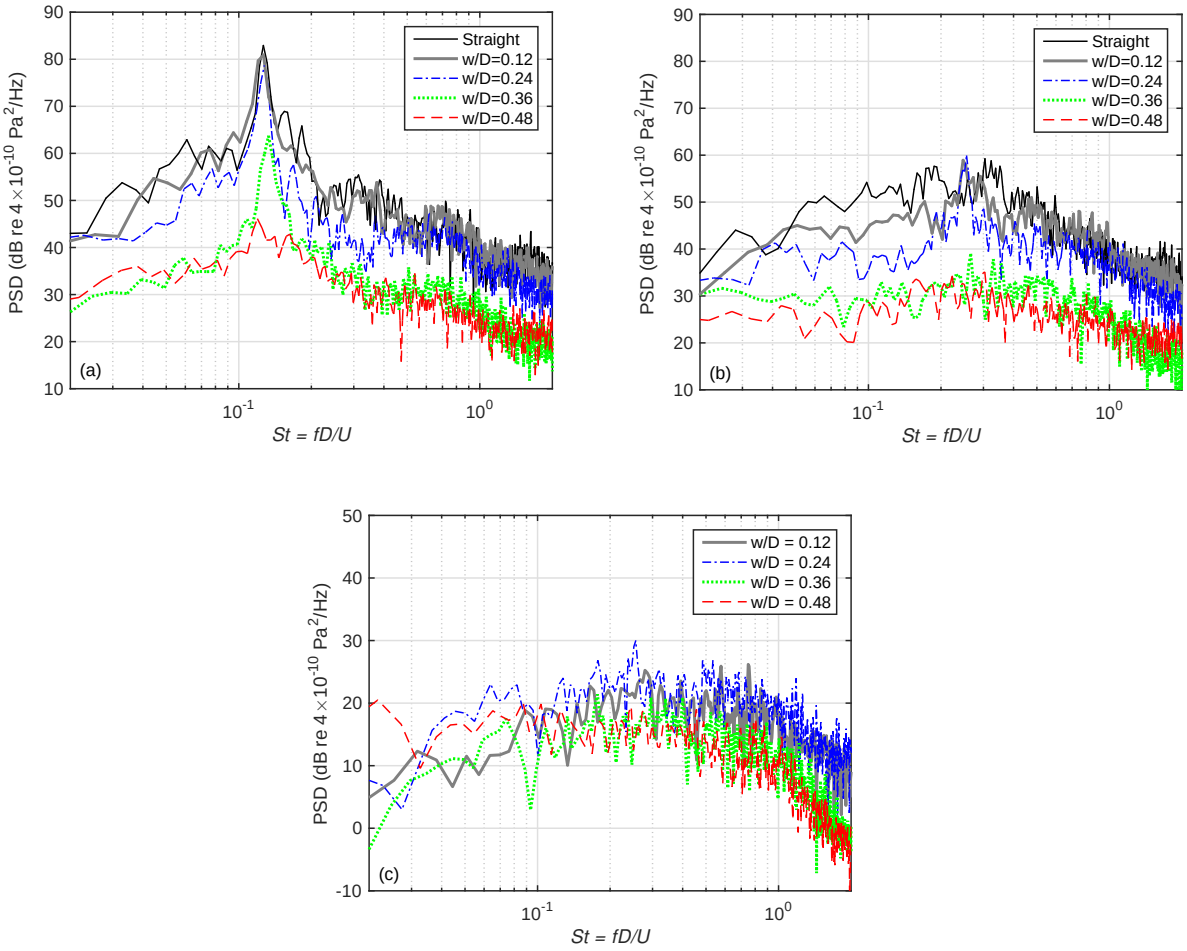

Figure 13: Computed far-field noise spectra at different receivers for $\lambda = 4D$ with different wave amplitudes. (a) $\theta = 90^\circ$ in $x-y$ plane. (b) $\theta = 180^\circ$ in $x-y$ and $x-z$ plane. (c) $\phi = 90^\circ$ in $x-z$ plane.

OASPL for $\lambda = 4D$ is 3.4 dB lower than for $\lambda = 2D$. This is consistent with the variations found in the PSDs of the drag coefficients in Figure 10. Significant noise reductions occur at $w/D = 0.36$, which are about 18 dB lower relative to the straight case for both the maximum and the minimum OASPLs. Increasing the amplitude from $w/D = 0.36$ to 0.48, the maximum OASPLs are reduced by a further 11 dB while the minimum OASPL only shows a 3 dB reduction. The differences between the maxima and the minima are $10 \sim 14$ dB for $w/D \leq 0.36$ and 6 dB for $w/D = 0.48$.

In the $x-z$ plane, the maxima are in the drag direction, and the minima are in the spanwise direction. The levels at $\phi = 90^\circ$ and 270°, influenced by the spanwise force fluctuations, are higher for the straight bar than the wavy cases. However, when w/D is increased from 0.12 to 0.48, the levels in the spanwise direction are reduced by 9 dB. The differences between the maxima and the minima in the $x-z$ plane for different wavy cases are in the range $14 \sim 25$ dB.

Table 4: The tonal peak level and the OASPL for the straight and wavy cases at different receivers .

Case	tonal peak level (dB/Hz) $\theta = 90°$	OASPL (dB) $\theta = 90°$	$\theta = 180°$	$\phi = 90°$
Straight	82.9	94.9	82.2	34.5
$\lambda = 4D$, $w/D = 0.12$	80.9	94.2	79.6	52.4
$\lambda = 4D$, $w/D = 0.24$	78.7	90.3	76.3	54.3
$\lambda = 4D$, $w/D = 0.36$	63.8	76.3	62.9	47.3
$\lambda = 4D$, $w/D = 0.48$	–	65.8	60.4	45.8
$\lambda = 2D$, $w/D = 0.12$	82.5	93.8	77.7	–
$\lambda = 2D$, $w/D = 0.24$	80.2	91.6	74.3	–
$\lambda = 2D$, $w/D = 0.36$	64.2	78.7	68.7	–

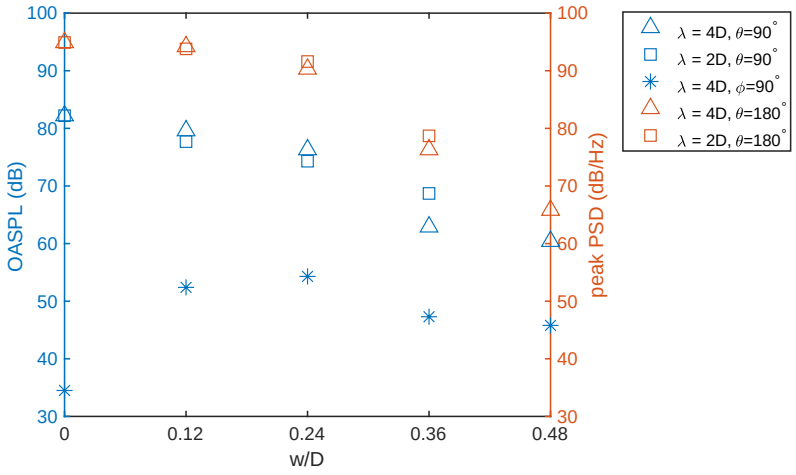

Figure 14: Variations of the OASPL and the tonal peak level with the wave amplitude at different receivers.

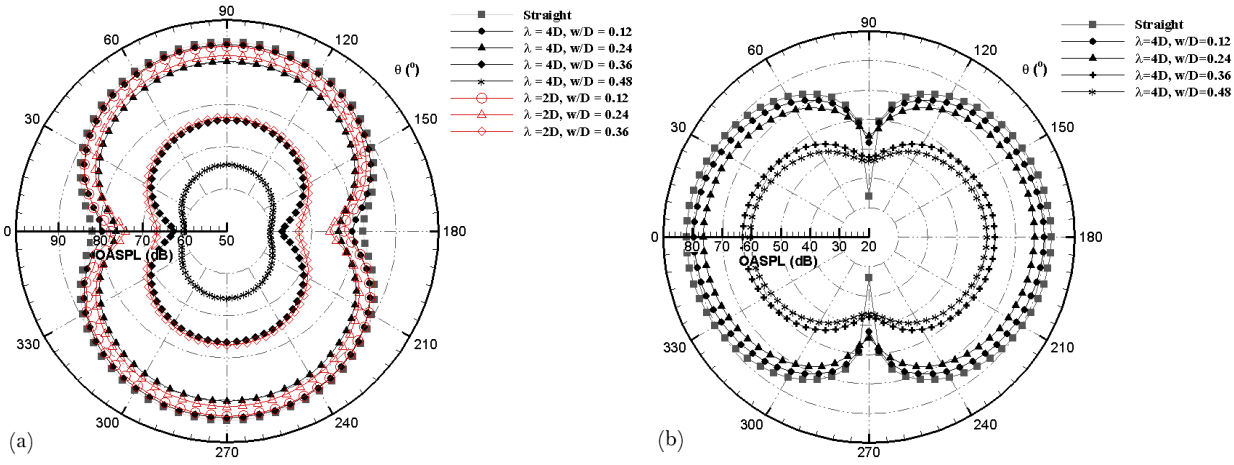

Figure 15: Computed far-field noise directivity for the straight case and different wavy cases. (a) $x-y$ plane. (b) $x-z$ plane.

5. Experimental validation

5.1. Experimental set-up

Measurements of radiated noise from square bars with spanwise waviness were carried out in the ISVR anechoic chamber (8 m×8 m×8 m), in which an open jet wind tunnel is set up as shown schematically in Figure 16(a). The chamber walls are acoustically treated with glass wool wedges. The open jet nozzle has a large contraction ratio of 25:1, which can reduce lateral velocity fluctuations and hence reduce the turbulence level at the jet exit. The nozzle rectangular exit area is 0.15 m × 0.45 m. This facility provides a high speed flow (up to 80 m/s) with low background noise and low turbulence intensity (0.4%) [49]. In the current work, measurements were carried out for four models, which are a straight square bar and wavy square bars with $\lambda = 2D$ and $w/D = 0.36$, $\lambda = 2D$ and $w/D = 0.48$, and $\lambda = 4D$ and $w/D = 0.48$, as shown in Figure 16(b). They are made of dense foam with a dimension of $D = 0.0225$ m and a spanwise length of $20D$ (0.45 m), which is the same as the nozzle exit width. For each bar, five speeds, $U = 20, 30, 40, 50$ and 60 m/s, corresponding to $Re = 3 \times 10^4 - 9 \times 10^4$, were tested to find the speed dependence and to assess the Reynolds number effect. The bars were positioned 0.15 m downstream of the nozzle to ensure that the entire bar is located well within the jet potential core, where the velocity deficit is small [49]. In order to maintain 2-D flow, two end-plates with the dimensions of $7.6 \times 11D$, made of clear acrylic with a thickness of 6 mm, were mounted to the sides of the nozzle exit and the bar was fixed between the end-plates, as can be seen in Figure 16. Although the end-plates may have some effect on the radiated sound, it is expected that the sound from a long bar is mainly radiated in the streamwise and crossflow directions. The influence of the end-plates on the radiated noise at the measurement locations is therefore expected to be relatively small. Absorptive material was placed on the ground and on the top of the nozzle to minimize sound reflections.

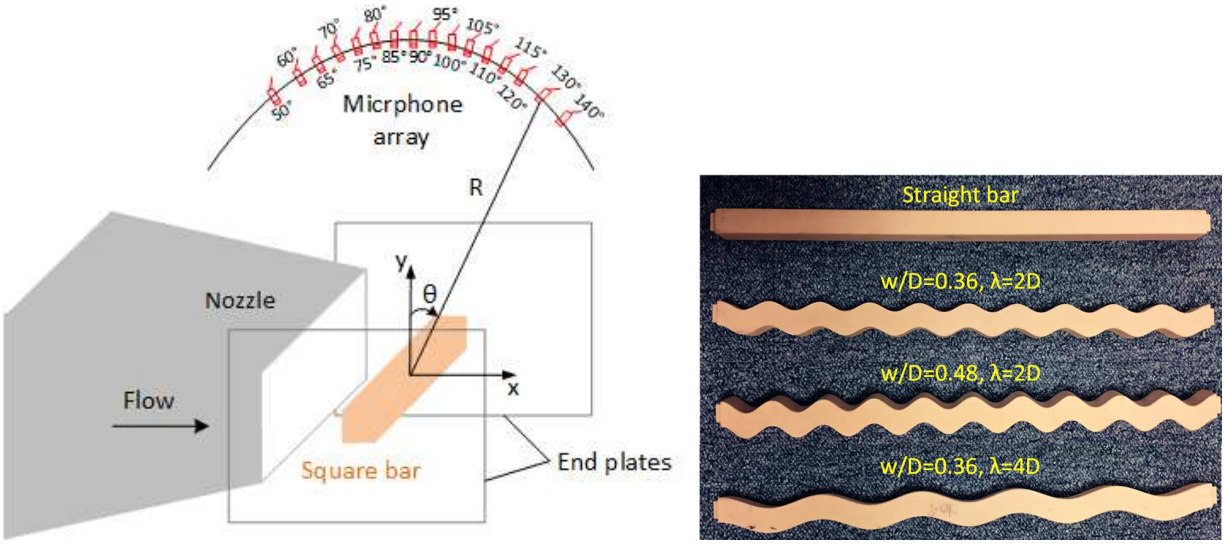

(a) (b)

Figure 16: (a) Experimental set-up sketch for noise measurements in the ISVR's anechoic chamber. (b) Tested bar models.

A set of microphones (B&K type 4189) was located in a plane parallel to the inflow direction and perpendicular to the bar axis at a radial distance $R = 1.18$ m ($52D$) from the bar, as indicated in Figure 16(a). The distance from the microphones to the bar is about three times the bar span, and corresponds to $52D$ from the bar. 16 microphones were distributed to cover a range of radiation angles, $\theta = 50° - 140°$. For each case, a time signal of 10 s duration was acquired at a sampling frequency of 50 kHz.

5.2. Experimental results

Measured narrow-band pressure PSDs at $\theta = 90°$ (as indicated in Figure 16(a)) are shown in Figure 17 for the straight and wavy bars at $U = 30$ and 60 m/s. The PSDs were calculated based on Welch's method using a Hanning

window of 16384 samples, resulting in a frequency resolution of around 3 Hz, with 50% overlap of the segments. This corresponds to a Strouhal number resolution of around 0.002 at 30 m/s and 0.001 for 60 m/s. For each spectrum, the background noise has been subtracted. The background noise, also shown in the figures, was measured when all the equipment was present except for the bar itself. It has been found that, for all cases, the spectral peaks were unaffected by the background noise, and it only has an influence at frequencies several times lower than the vortex shedding frequency. The background noise was found to affect a wider range of Strouhal numbers for the wavy models with high amplitude, $w/D = 0.48$ as the radiated noise is much lower. Therefore, when calculating the OASPL, the PSDs are integrated over frequency in the range of $St = 0.07 - 2$ to ensure that the most significant information is contained and at the same time, the influence from the background noise is minimized.

From Figure 17, it is found that, compared with the straight case, a significant reduction of 20 dB in the peak noise level is obtained for the case of $\lambda = 2D$ and $w/D = 0.36$. The noise levels at other frequencies are also reduced but by a smaller margin. When the wave amplitude is increased to $w/D = 0.48$, the noise spectra become broadband, especially for 60 m/s, and a further reduction of 15 dB is found in the peak level, whereas at other frequencies, the levels are nearly unchanged compared with $w/D = 0.36$.

Figure 17 also provides comparisons between the two wavelengths, $\lambda = 2D$ and $4D$, for $w/D = 0.48$. At $U = 30$ m/s, a broader spectral peak appears for $\lambda = 4D$ with a slightly higher frequency and the level is about 3 dB lower than for $\lambda = 2D$. At $U = 60$ m/s, the differences are less noticeable as the spectral peak for $\lambda = 2D$ becomes broader at this speed and the level is reduced to the same extent as for $\lambda = 4D$, although there is still 17% difference in the peak Strouhal number ($St = 0.109$ for $\lambda = 2D$, $St = 0.127$ for $\lambda = 4D$).

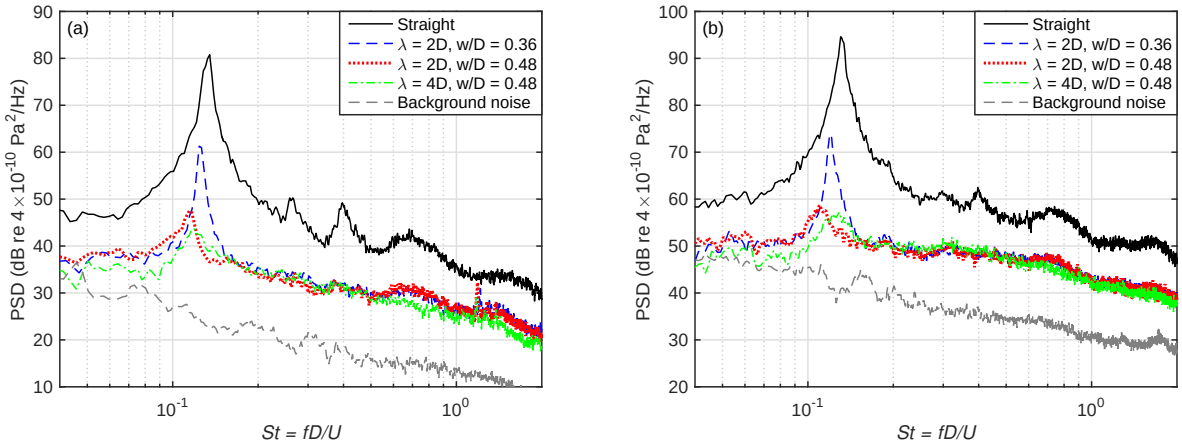

Figure 17: Narrow band measured PSDs at $\theta = 90°$. (a) $U = 30$ m/s. (b) $U = 60$ m/s.

Figure 18 shows the dependence of the tonal peak level and the OASPL on the flow speed for the different cases. The tonal peak level is obtained from the peak of the 1/6 octave band spectrum. These results are from the receiver at $\theta = 90°$. The speed exponent was obtained from the slope of the straight line that best fits the results. Different speed exponents are found for the straight and wavy bars, which vary from 5.0 to 5.8 for the tonal peak level and 5.3 to 6.1 for the OASPL. The speed exponents for the wavy cases obtained from the 1/6 octave peak SPL are generally lower than those from the OASPL. This is consistent with the findings that the peak becomes broader and the levels at $St \geq 0.2$ become higher with increased speeds, as will be shown later. It is also found from Figure 18 that the differences in both the tonal peak level and the OASPL caused by different wavelengths, $\lambda = 2D$ and $4D$ at $w/D = 0.48$, are insignificant, with the maximum difference found at 20 m/s, which is only 2.4 dB for the tonal peak level and 1.2 dB for the OASPL.

The noise reduction induced by the waviness relative to the straight bar for the tested Reynolds numbers is shown in Figure 19. The reductions in both the tonal peak level and the OASPL are presented. It can be seen that for the wave amplitude of $w/D = 0.36$, the reductions in the OASPL are similar to those in the tonal peak level, at around

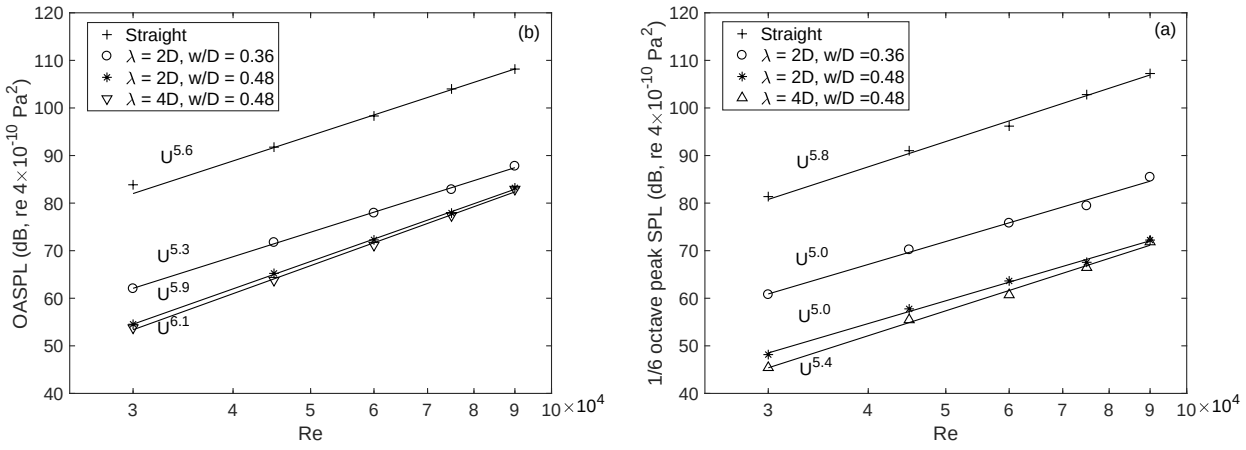

Figure 18: The dependence of the measured 1/6 octave band peak SPL (a) and the OASPL (b) on the flow speed.

21 dB, while for $w/D = 0.48$, the OASPL reductions are generally smaller than the peak level reductions, especially for higher Reynolds numbers. For $w/D = 0.48$, the reduction in the peak level shows small variations with varying Reynolds number, at around -34 dB, while the reduction in the OASPL appears to become smaller with increased Reynolds numbers, varying from about 30 dB at 20 m/s to 25 dB at 60 m/s.

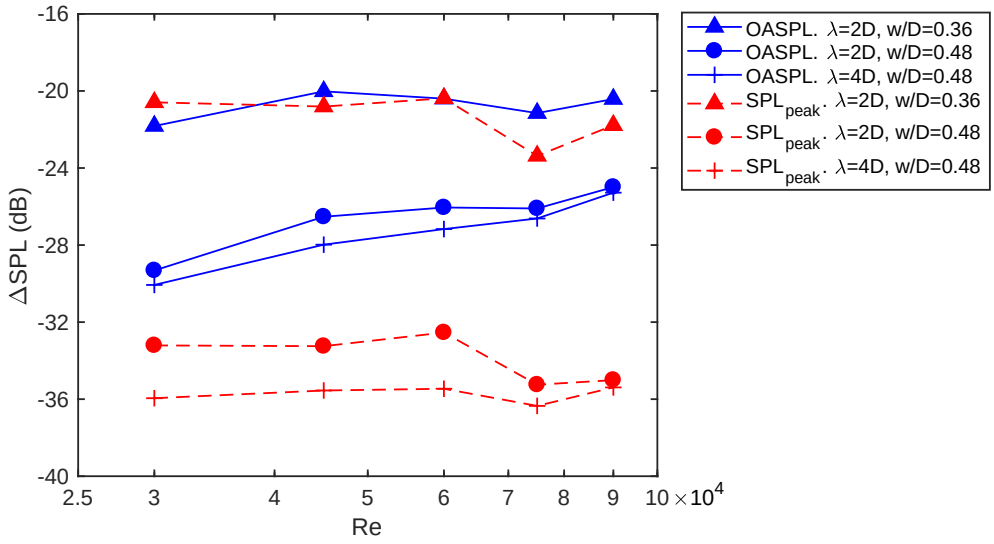

Figure 19: Noise reduction levels, represented by ΔSPL as a function of speed for different wavy cases. ΔSPL is calculated from the OASPL, or the 1/6 octave peak SPL, for the wavy cases relative to the corresponding straight case.

5.3. Comparisons between experimental and computational results

The far-field 1/6 octave band noise spectra are compared between the measurements at $Re = 3 \times 10^4 - 9 \times 10^4$ and the simulation results at $Re = 1.64 \times 10^5$ in Figure 20. The receiver is located at $\theta = 90°$ (see Figure 16(a)), where the radiated noise is mainly influenced by the lift fluctuations. The measurement results were scaled by U_∞, D, L and R

according to the following equation to allow for direct comparisons with the simulated results,

$$\overline{p^2(r)} = \frac{\rho_0^2 U_\infty^6 St_p^2 C_{L,\mathrm{rms}}^2 L l_c D}{16 c_0^2 R^2} \tag{2}$$

where $\overline{p^2}$ is the far-field mean-square pressure, ρ_0 is the air density, c_0 is the sound speed and l_c is the spanwise correlation length normalized by D. This equation is derived from Curle's acoustic analogy for sources on the cylinder surface and illustrates the factors affecting the far-field pressure radiated from a solid cylinder [4], [50] and [51]. The narrow band spectra were then converted to 1/6 octave bands which are chosen to provide sufficient details of the spectral shape while allowing the spectra to be easily distinguishable.

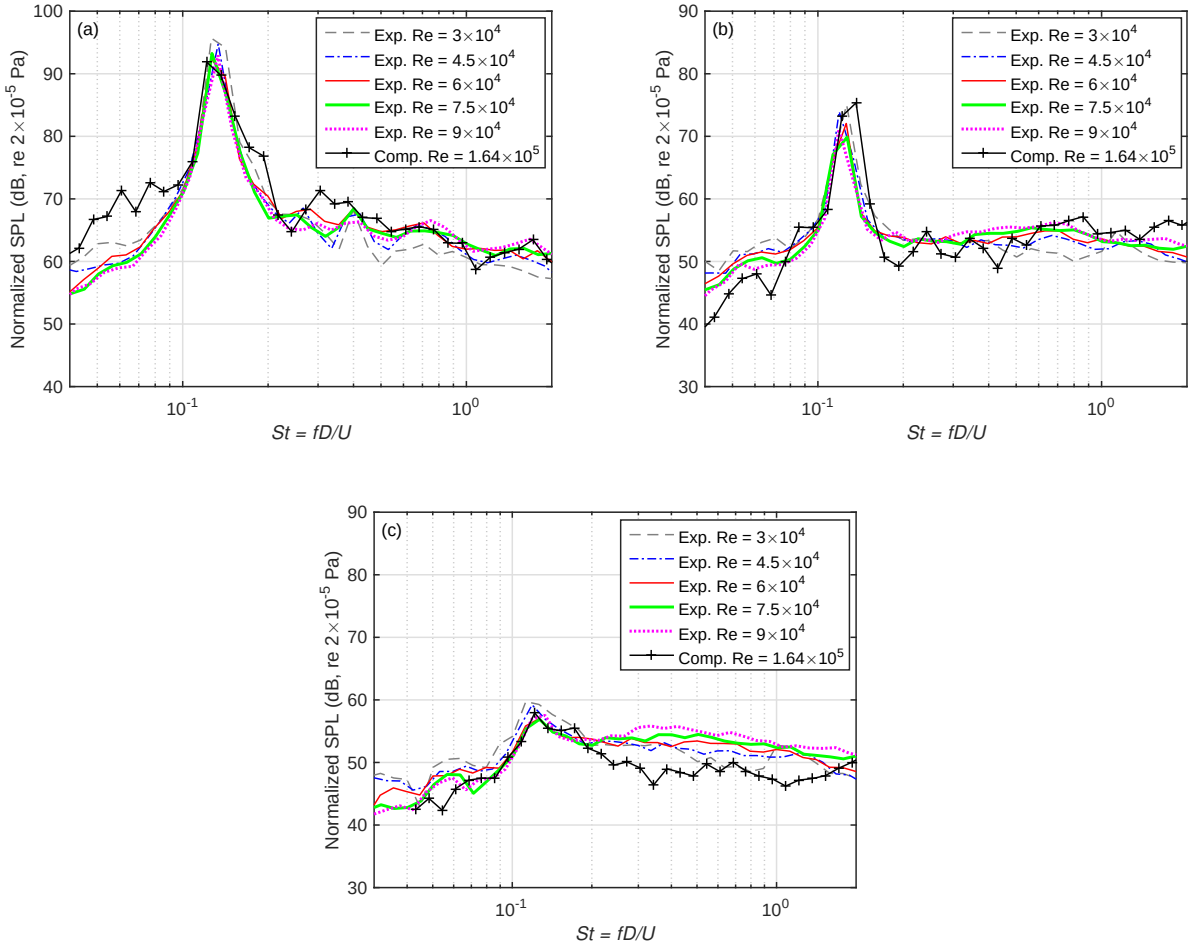

Figure 20: Comparisons of far-field 1/6 octave band noise spectrum between measurements and simulations. The measurement results has been normalized based on inflow speed U_∞, dimension D, spanwise length L and receiver distance R to allow comparisons with the computational results. (a) Straight. (b) $\lambda = 2D$ and $w/D = 0.36$. (c) $\lambda = 4D$ and $w/D = 0.48$.

Good agreement is found between the measurements and the simulation for both the straight and wavy cases. In Figure 20(a) for the straight case, the measurements show a variation of 2.5 dB in the peak level among different Reynolds numbers. The slight deviations in the peak Strouhal number are caused by the different central frequencies of the 1/6 octave bands for different speeds when expressed in terms of St. From the narrow band spectrum, it is found

that $St_p = 0.126$ from the simulation which is only about 4% smaller than $St_p = 0.131$ from the experiments. The peak level is also well predicted by the simulations, although the measured results may be slightly increased due to the presence of the end-plates. Simulations show higher spectral levels at low frequencies, $St = 0.03 - 0.09$ with a broad hump, which is also seen in the spectrum of the lift coefficient (Figure 7) and corresponds to a slow modulation with a period of 2 or 3 times the fundamental vortex shedding cycle. In Figure 20(b), for $w/D = 0.36$, a scatter of 4 dB is found in the peak levels from the measurements, while the peak level from the simulation is about 2 dB higher. For the peak frequency, a 6% deviation is found from the narrow band spectrum, with $St_p = 0.129$ for the simulation and $St_p = 0.122$ for the measurements. For $w/D = 0.48$ and $\lambda = 4D$, as shown in Figure 20(c), good agreement between the measurements and the simulations is obtained for both the peak frequency and the peak level, while the levels from the simulations are generally lower for $St \geq 0.2$. This is probably due to the mesh quality because the high waviness and the extrusion of the 2-D mesh along the span profile introduces higher skewness in the cells. In addition, it is found from the measurements that, with increasing Reynolds numbers, the levels at $St \geq 0.2$ gradually increase. This may suggest that at higher *Re*, a stronger 3-D turbulence interaction may occur in the wake which leads to an increase in the noise level at high frequencies, and thus the OASPL is increased as well. This will be further investigated in Section 6. From the above discussion, it is concluded that for the straight case and the wavy case with $w/D = 0.36$, the radiated noise is independent of Reynolds number over the range studied, while for $w/D = 0.48$, a small Reynolds number effect is found as the noise levels at high frequencies are affected, but the level and the frequency of the broadband peak are found to be unaffected.

Figure 21 shows the far-field noise directivity for the straight and wavy cases. The results are shown as ΔOASPL which is the OASPL at different receivers relative to the value at $\theta = 90°$. Since it has been found that the Reynolds number effect can be neglected in the current Reynolds number range, the measured results are also given in Figure 21 as the averaged value for all Reynolds numbers. In addition, a theoretical result for a lift dipole, $10\log_{10}\sin^2\theta$ is also plotted in the figure. A large dispersion in the results between different Reynolds numbers is found for the straight case and the wavy case of $\lambda = 2D$ and $w/D = 0.36$, which is more noticeable for receivers further away from $\theta = 90°$. For all the cases presented, the simulation shows good agreement with the averaged data from the measurements. The largest deviation between them is about 4 dB at $\theta = 50°$ for $\lambda = 2D$ and $w/D = 0.36$. In addition, the results show good agreement with the theoretical line for the straight case and the wavy case of $w/D = 0.36$, whereas for $w/D = 0.48$, the theoretical results are noticeably lower at the receivers further away from $\theta = 90°$. This is due to the fact that the difference between the levels of the drag and the lift dipoles reduces for $w/D = 0.48$. Further away from $\theta = 90°$, the drag dipole will have a greater contribution which needs to be taken into account.

6. Flow features analysis

As discussed above, the noise radiated from a square bar can be significantly reduced by introducing spanwise waviness with large wave amplitudes, e.g. $w/D = 0.36$ and 0.48. The flow physics is analysed here to establish the associated noise reduction mechanisms. All the flow results presented in this section are obtained from the numerical simulations described in Sections 3 and 4. As the effect of the wavelength was found to be small, especially on the noise induced by the lift dipole, the following analysis will focus on flow features for different wave amplitudes at a fixed wavelength $\lambda = 2D$.

6.1. Instantaneous flow structures

The instantaneous flow structures for the wavy bar cases with different wave amplitudes are shown in Figure 22 and compared with the corresponding results for the straight bar. These are represented by the iso-surfaces of the normalized Q-criterion. The normalized value Q_n is given by $Q_n = Q/(U_\infty/D)^2$, where Q is the second invariant of the velocity gradient tensor which can be calculated by $Q = \frac{1}{2}(\Omega_{ij}\Omega_{ij} - S_{ij}S_{ij})$, where $S_{ij} = \frac{1}{2}(\frac{\partial u_i}{\partial x_j} + \frac{\partial u_j}{\partial x_i})$ is the strain rate and $\Omega_{ij} = \frac{1}{2}(\frac{\partial u_i}{\partial x_j} - \frac{\partial u_j}{\partial x_i})$ is the rotation rate. Detailed structures can be well identified from these Q-criterion plots, which confirms confidence of the grid resolution in the current simulations. As can be seen, the straight bar exhibits a strong alternating periodic vortex shedding which also appears for the wavy bar with a small amplitude $w/D = 0.12$. When the amplitude is increased to $w/D = 0.36$, the coherent vortex shedding is suppressed as the separated shear layer only starts to interact and rolls up into the primary vortex farther downstream. Further increasing the waviness to $w/D = 0.48$, the coherent vortex shedding becomes difficult to identify. These plots also show the development of

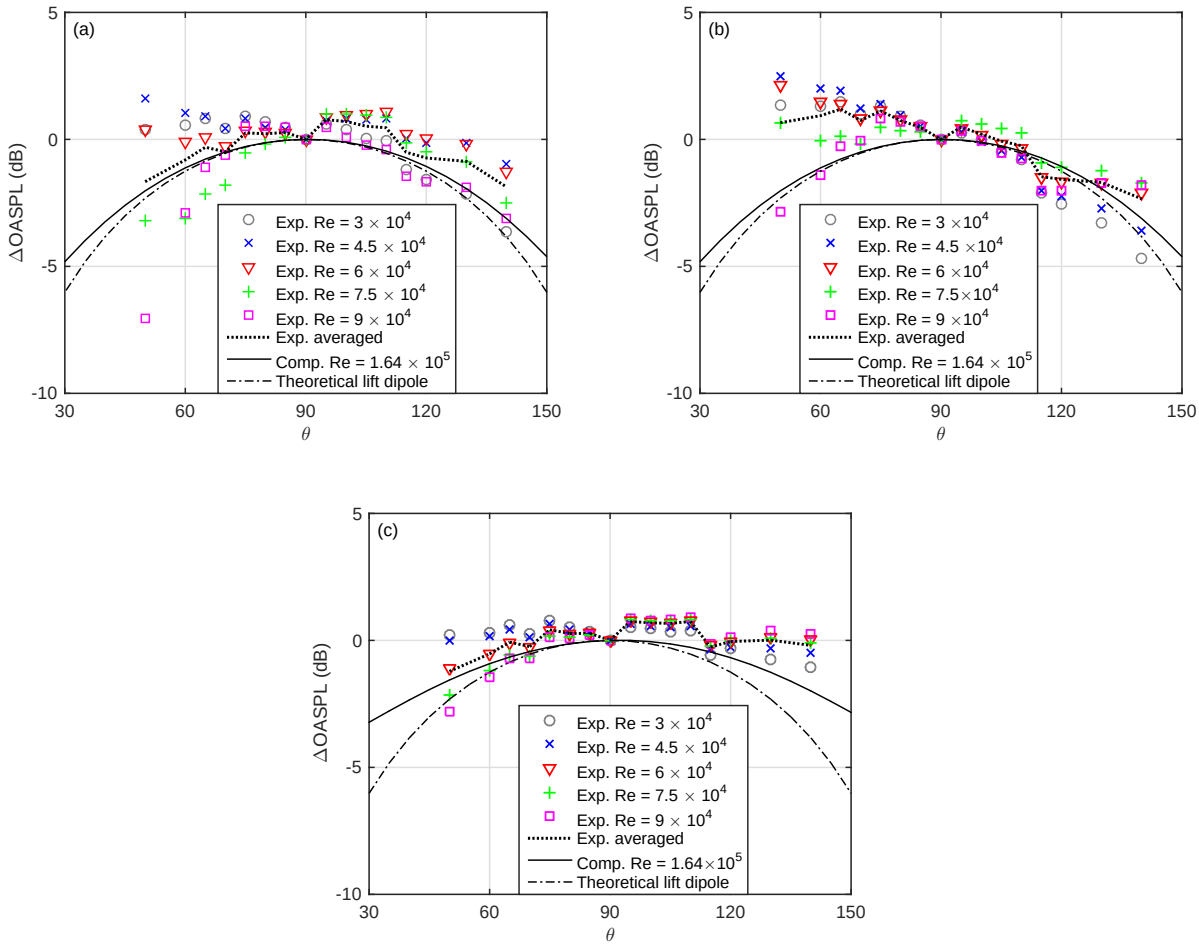

Figure 21: Comparisons of far-field noise directivity between measurements and simulations. (a) Straight. (b) $\lambda = 2D$ and $w/D = 0.36$. (c)$\lambda = 4D$ and $w/D = 0.48$.

small secondary vortices which appear rapidly after flow separation and then break down into 3-D structures after a short distance. These secondary vortices are generated by the shear layer instability, which can speed up the transition from laminar to turbulent flow [52]. The waviness promotes the secondary instability and causes the break down into 3-D structures to happen earlier, by generating spanwise motion. The secondary vortices are found to follow the wavy shape of the bar for $w/D = 0.36$ and 0.48.

Figure 23 shows the instantaneous distributions of the divergence of the Lamb vector in the $x - y$ plane at the peak and the valley (as indicated in Figure 6(a)). The Lamb vector is defined as $\boldsymbol{\omega} \times \mathbf{u}$, where $\mathbf{u}$ is the velocity vector and $\boldsymbol{\omega} = \nabla \times \mathbf{u}$ is the vorticity. The negative and positive values of its divergence represent strong vorticity regions and strong strain regions respectively, and the switch between the negative and positive values can influence the momentum transfer [53]. The mechanisms related to the Lamb vector divergence play an important role in the evolution of the shear layer separated from the bar. For the straight bar, a strong interaction is observed behind the bar. When span waviness is introduced, the distribution of the Lamb vector divergence varies at different spanwise locations; results are shown at the peak and the valley in Figure 23. The width between the two separated shear layers is found to increase at the valley and decrease at the peak, which is especially apparent at the larger wave amplitudes.

In addition, according to Hamman et al. [53], the interaction between regions of negative and positive Lamb vector

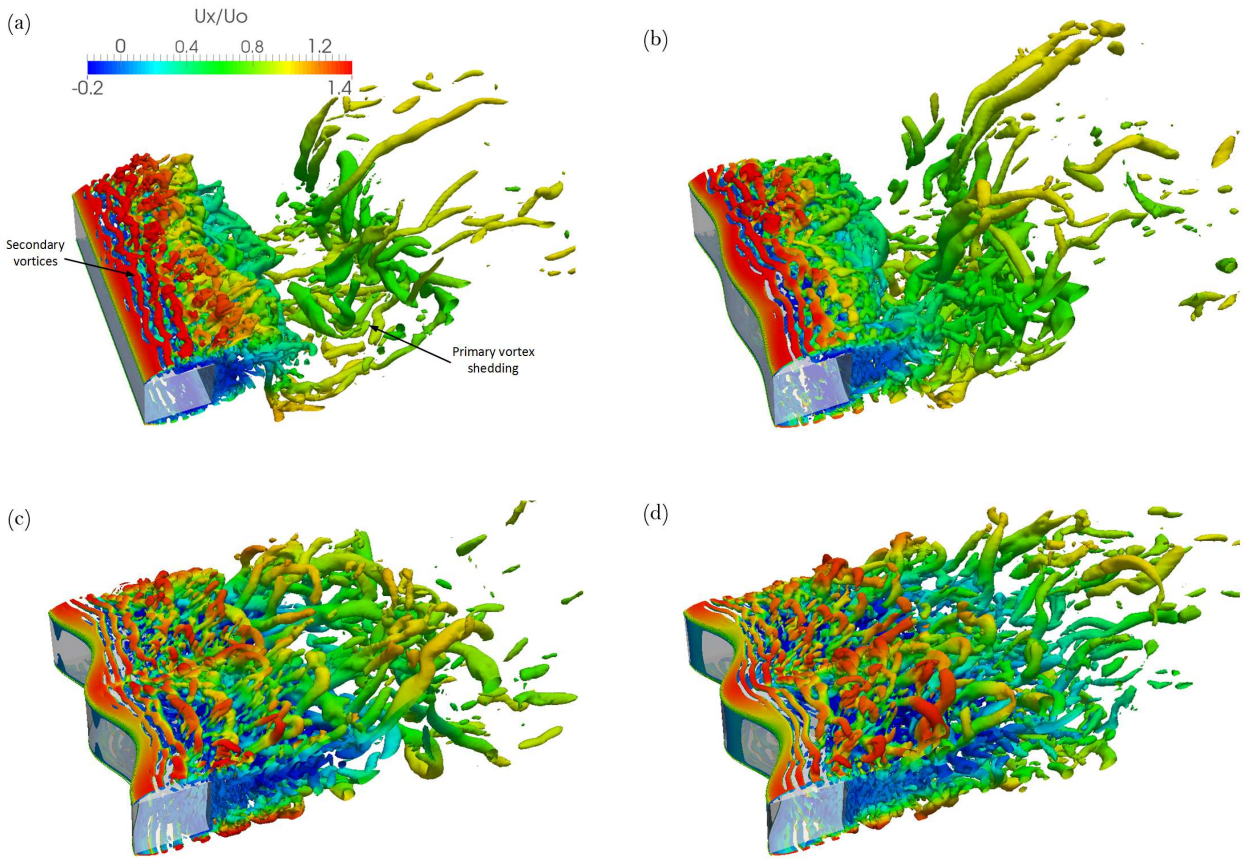

Figure 22: The iso-surface of instantaneous normalized Q-criterion, with $Q_n = 6$, which is coloured by the normalized mean streamwise velocity, U_x/U_∞. (a) Straight. (b) $w/D = 0.12$. (c) $w/D = 0.36$. (d) $w/D = 0.48$.

divergence is also related to the forces on a body. Hamman et al. [53] found that reducing the size of the interaction regions of the positive and negative Lamb vector divergence leads to a reduction in drag. From the current simulations, it can be seen that the interaction of the Lamb vector divergence appears to be concentrated intensively behind the straight bar. Introducing waviness with a small amplitude $w/D = 0.12$ does not make a significant difference to this. However, when the amplitude is increased to $w/D = 0.36$, the interaction between regions of positive and negative Lamb vector divergence becomes much weaker in the near wake of the bar, especially in the plane cut through the valley, while for the peak plane it occurs slightly further downstream compared with the straight and $w/D = 0.12$ wavy case. Further increasing the amplitude to $w/D = 0.48$, the interaction becomes weaker in both the peak and the valley planes. Hence, the drag is expected to reduce with increased wave amplitudes. In addition, the Lamb vector divergence is the source term for vortex generated sound [54]; reducing the Lamb vector divergence reduces the noise source and would lead to a reduction in radiated noise. From the above discussions, it is therefore expected that the radiated noise is weakened for the wavy bars with high wave amplitudes.

6.2. Mean flow properties

The vortex formations in the wake region at the peak and the valley are shown in Figure 24 by the mean flow streamlines. For all the cases, as the mean flow is symmetric about the centreline, only half of the plane is presented for each case. The top half corresponds to the peak plane while the bottom half is for the valley plane. These results clearly illustrate the variations in the vortex formation length and the wake width at different spanwise locations when waviness is introduced along the span. The change in the vortex formation length between the straight case and the

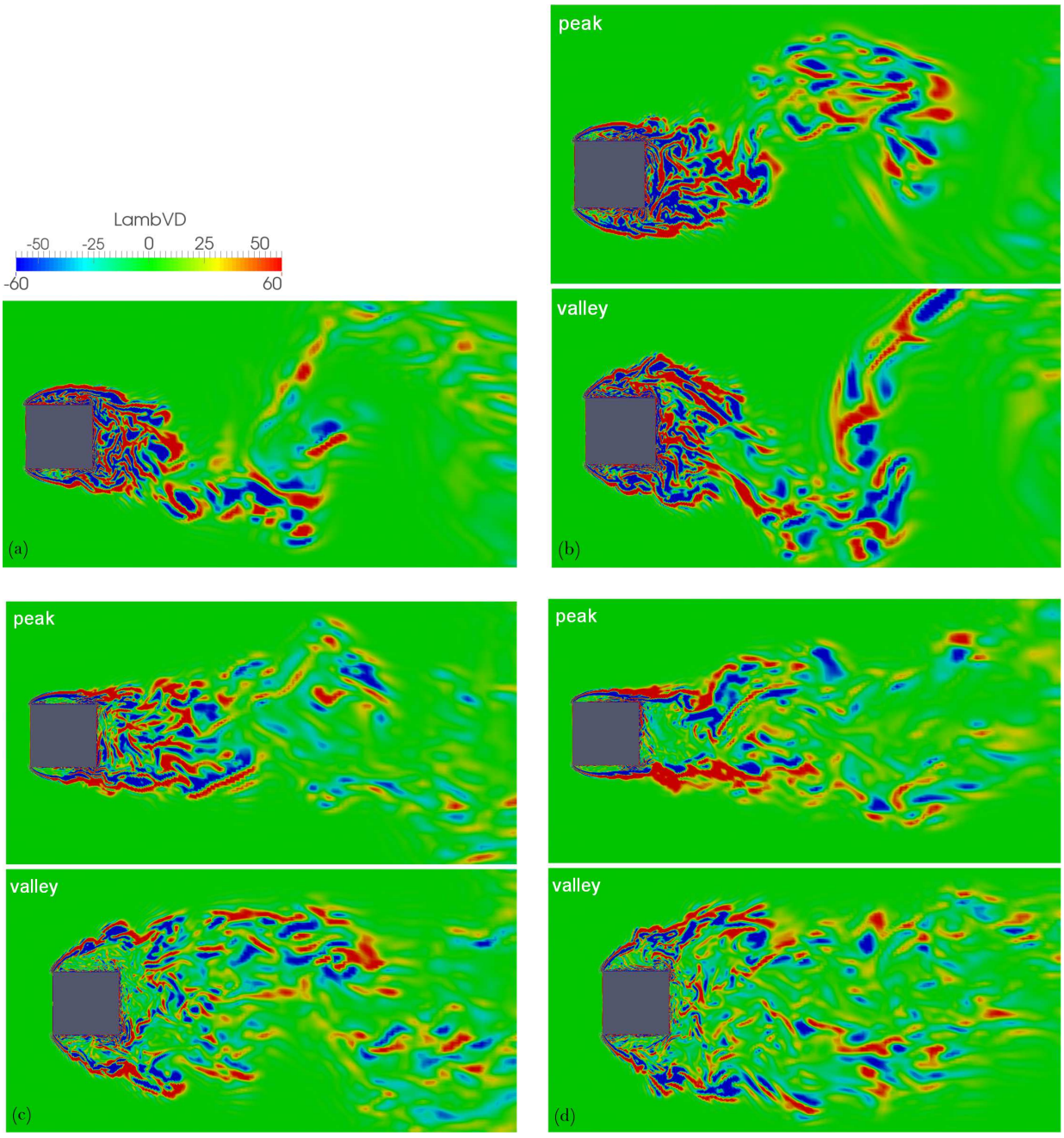

Figure 23: The instantaneous distributions of the divergence of the Lamb vector in the $x-y$ plane at the peak (top) and the valley (bottom). (a) Straight. (b) $w/D = 0.12$. (c) $w/D = 0.36$. (d) $w/D = 0.48$.

case with $w/D = 0.12$ is very small; similar values are therefore obtained for C_D and $C_{L,rms}$. However, for larger waviness amplitudes, $w/D = 0.36$ and 0.48, significant changes can be seen in the vortex formation at both the peak and the valley planes. In the valley plane, the vortex formation is significantly lengthened for both $w/D = 0.36$ and 0.48, while in the peak plane, the fundamental vortex formation is distorted by the spanwise motion introduced by the high wave amplitude; especially for $w/D = 0.48$ there is no fundamental vortex formation. It is known that the values

of C_D, $C_{L,rms}$ and $C_{D,rms}$ are highly related to the fundamental vortex formation; hence much reduced C_D, $C_{L,rms}$ and $C_{D,rms}$ are expected, for $w/D = 0.36$ and 0.48, which were also confirmed in Figure 11.

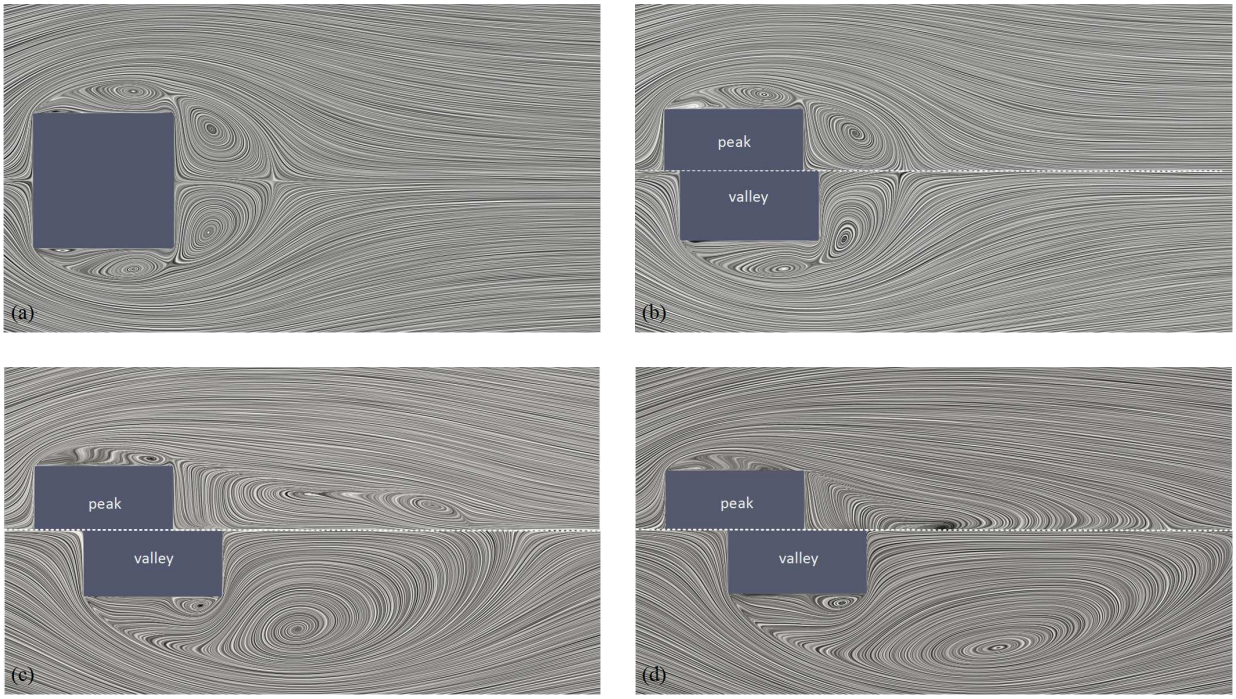

Figure 24: Mean flow streamlines in the $x-y$ plane at the peak (top half) and the valley (bottom half). (a) Straight. (b) $w/D = 0.12$. (c) $w/D = 0.36$. (d) $w/D = 0.48$.

Figure 25 shows the distributions of the TKE at the peak and valley planes. For the straight case, a strong TKE region first appears almost directly above the rear corner of the bar and later along the centreline around the closure of the vortex formation. Similar TKE profiles are also found for $w/D = 0.12$ although the area of large TKE is increased at the peak and decreased in the valley. When the amplitude is increased to $w/D = 0.36$ and 0.48, the levels of the TKE are significantly reduced and changes in its distribution can be clearly recognized in both the peak and valley planes. For both $w/D = 0.36$ and 0.48, the levels of the maximum TKE are much smaller, although in the peak plane they are higher than those in the valley plane. This is due to the more intense momentum exchange in the peak regions as significant spanwise flow at the back of the bar is introduced by the wavy shape. The fluid moves from the valley and converges at the peak and this spanwise motion breaks the large coherent structures of vortex shedding, as will be shown later. For $w/D = 0.36$, the maximum TKE in the peak plane tends to occur away from the centreline and appears much further downstream of the bar compared with the straight bar, while in the valley plane, it occurs in the separated shear layer. This is more apparent for $w/D = 0.48$. These discussions indicate that the turbulence interactions are greatly weakened for $w/D = 0.36$ and 0.48 which explains the reductions in the force fluctuations as well as the noise levels at other frequencies in addition to the peak frequency.

As already noted, unlike the straight bar, the wavy bars show variations in the wake width along the span and these variations become more pronounced with increased wave amplitudes. This may be associated with the changes in the regions of favourable and adverse pressure gradients. The mean pressure coefficient distribution around the bar surface at the peak and the valley is presented in Figure 26. The slope of the curve indicates the pressure gradient. A negative value represents a favourable pressure gradient, which enables the flow acceleration. It can be seen that on the windward side (AB), the wavy bars present a more significant favourable pressure gradient at the valley than at the peak. This implies that the flow acceleration on the windward side will be stronger at the valley, which will then result in a higher crossflow (y) velocity. Conversely, the smaller favourable pressure gradient at the peak leads to a lower crossflow (y) velocity. The variation in the crossflow velocity along the span contributes to the widening

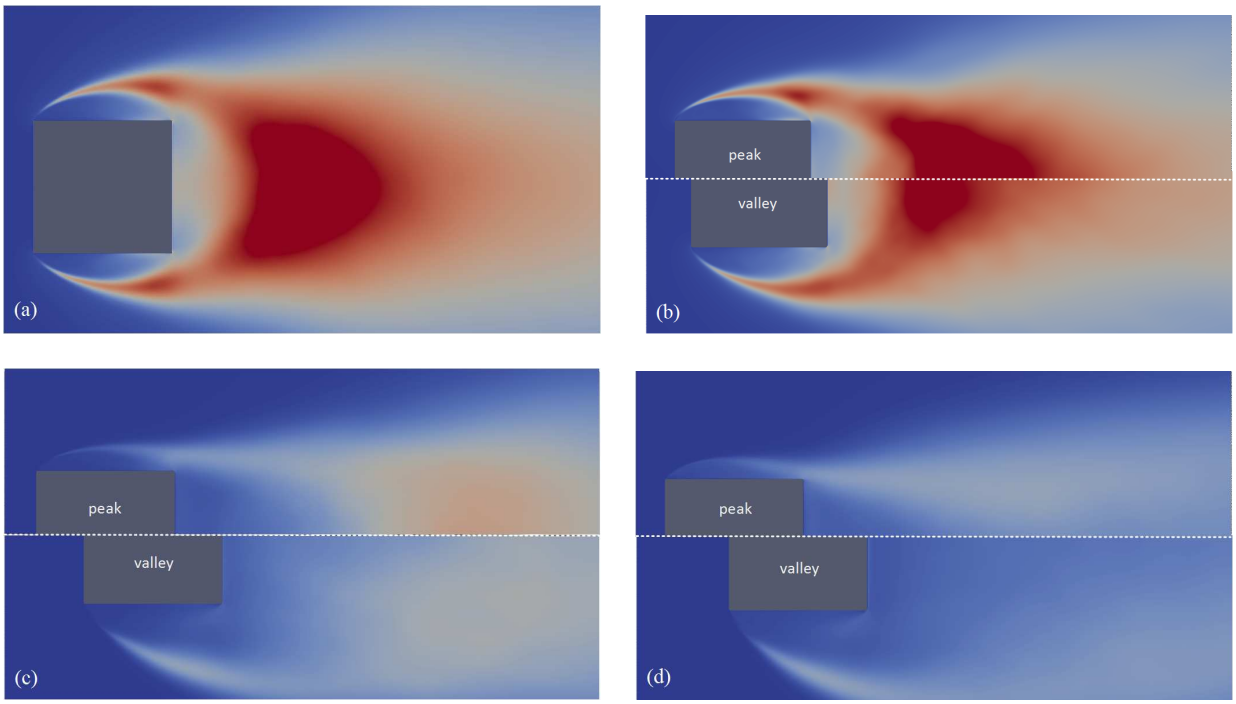

Figure 25: Normalized turbulent kinetic energy distributions in the $x-y$ plane at the peak (top half) and the valley (bottom half). (a) Straight. (b) $w/D = 0.12$. (c) $w/D = 0.36$. (d) $w/D = 0.48$.

and narrowing of the near wake. The difference in the pressure gradient between the peak and the valley is more noticeable with increased waviness amplitudes. Introducing the spanwise waviness also influences the back pressure distribution. As can be seen in Figure 26, with increased wave amplitudes, the back pressure (on side CD) increases, which results in decreased drag coefficients.

To understand the 3-D flow development, the mean 2-D flow streamlines in the $x-z$ and $y-z$ planes are plotted in Figure 27. The $x-z$ and $y-z$ planes are coloured by the normalized mean cross-flow vorticity ($\omega_{yn} = \frac{\omega_y D}{U_\infty}$, where $\omega_y = \frac{\partial u}{\partial z} - \frac{\partial w}{\partial x}$) and streamwise vorticity ($\omega_{xn} = \frac{\omega_x D}{U_\infty}$, where $\omega_x = \frac{\partial w}{\partial y} - \frac{\partial v}{\partial z}$) respectively to understand the redistribution of the vorticity. The $x-z$ plane is located at $y/D = 0.64$ which is $0.14D$ above the bar, while the $y-z$ plane is located at $x/D = 0.64$ which is just $0.14D$ behind the rear surface of the bar. As can be seen, for the straight case, there is no presence of streamwise or crossflow vortices and the streamlines in both planes are 2-D. When the spanwise waviness is introduced with a small amplitude, $w/D = 0.12$, the streamlines in both planes tend to become 3-D. ω_y appears with weak strength just after the flow separation in the $x-z$ plane and follows the bar wave shape. When the wave amplitude is further increased to $w/D = 0.36$, two pairs of streamwise and crossflow vortices with high strengths form at the rear of the peak region in the $y-z$ and $x-z$ planes respectively and they are symmetric about the peak plane. This implies that the spanwise vorticity (ω_z) is transported into the other two components, ω_x and ω_y, for this high waviness amplitude, through spanwise motion interacting with the vortices. Further increasing the amplitude to $w/D = 0.48$, the streamwise and crossflow vortices at the rear of the peak region appear to grow and the strengths of ω_x and ω_y become greater. In addition, the crossflow vortex pairs (which are shielded by the bar and thus are invisible in the current plots) with strong strengths of ω_y are also found in the wake of the peak region for both $w/D = 0.36$ and 0.48. The redistribution of the vorticity from spanwise into streamwise and crossflow directions caused by the spanwise waviness makes it difficult for the separated shear layer to interact and roll up into the fundamental vortex, hence resulting in a much suppressed vortex shedding.

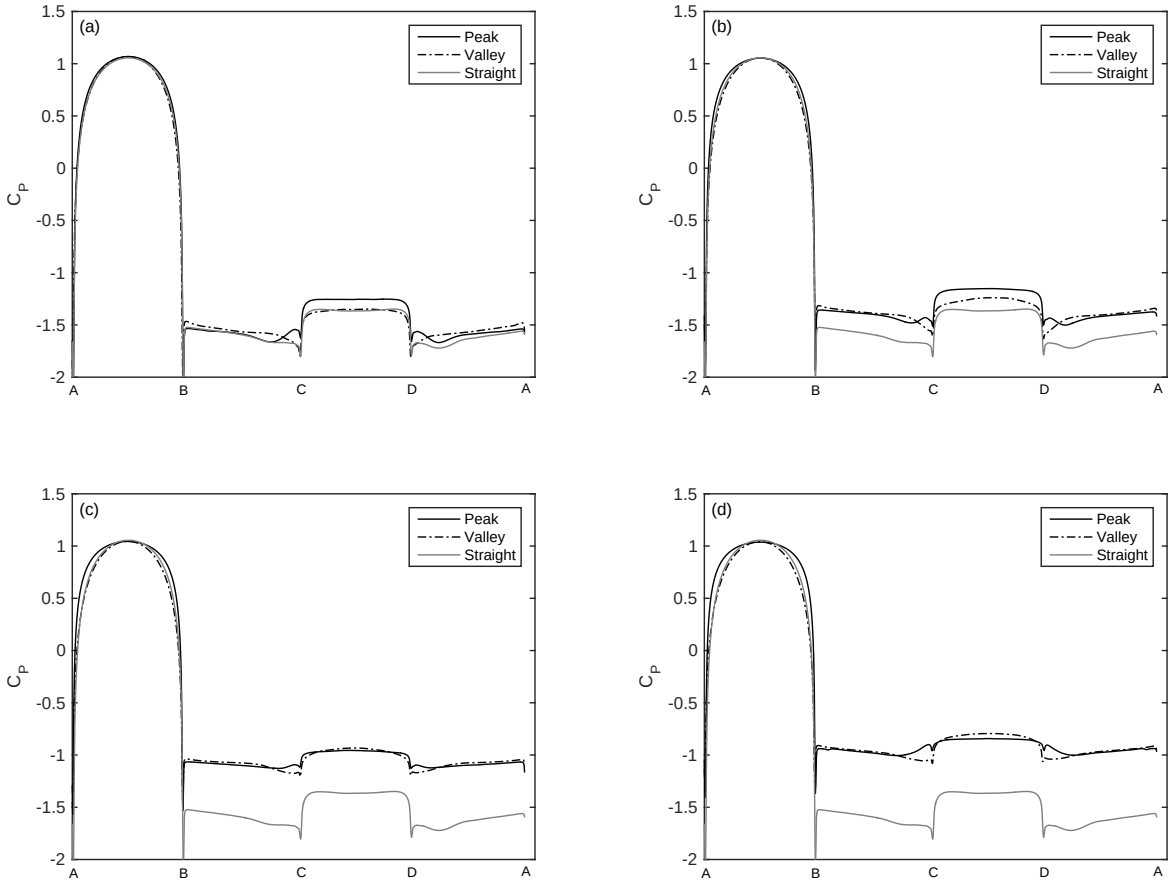

Figure 26: Mean pressure coefficient distribution around the wavy bar surface at the peak (−) and the valley (−.) compared with the straight bar. (a) $w/D = 0.12$. (b) $w/D = 0.24$. (c) $w/D = 0.36$. (d) $w/D = 0.48$.

7. Conclusions

In the present study, both numerical simulations and noise measurements have been conducted to investigate the reduction of aerodynamic noise from square bars by introducing spanwise waviness. Good agreement has been obtained between the numerical simulations and the noise measurements in terms of the far-field noise spectra. Regarding the flow aerodynamics, significant reductions are found in the values of C_D, $C_{L,rms}$ and $C_{D,rms}$ when the waviness amplitude is increased to $w/D = 0.36$ or higher. For $w/D \leq 0.24$, the reductions are much smaller for C_D and $C_{L,rms}$, but still noticeable for $C_{D,rms}$. The peak Strouhal number is found to be much less sensitive to the spanwise waviness for $w/D \leq 0.36$, while for $w/D = 0.48$, the spectral peak becomes much weaker and broadband and the frequency corresponding to the maximum level is difficult to identify. The variations in C_D, $C_{L,rms}$ and $C_{D,rms}$ are consistent for different wavelengths, $\lambda = 2D$ and $4D$, although some differences are found in $C_{D,rms}$ especially for $w/D \geq 0.36$.

Aerodynamic noise is generated by flow unsteadiness; thus the aerodynamic noise radiated from bars is directly related to the above aerodynamic parameters. Therefore a significant noise reduction is expected for high waviness amplitudes. This has been confirmed both numerically and experimentally in the present study. It was found that the tonal peak for a receiver at $\theta = 90^\circ$, dominated by the lift fluctuations, was reduced by up to 36 dB when going from the straight case to $w/D = 0.48$. In addition to this, considerable reductions in the levels at other, both lower and higher, frequencies are also obtained. The maximum reduction in the measured OASPL reaches 30 dB for $Re = 3 \times 10^4$. Increasing the Reynolds number from 3×10^4 to 9×10^4 has little effect on the reduction of the tonal noise, but the

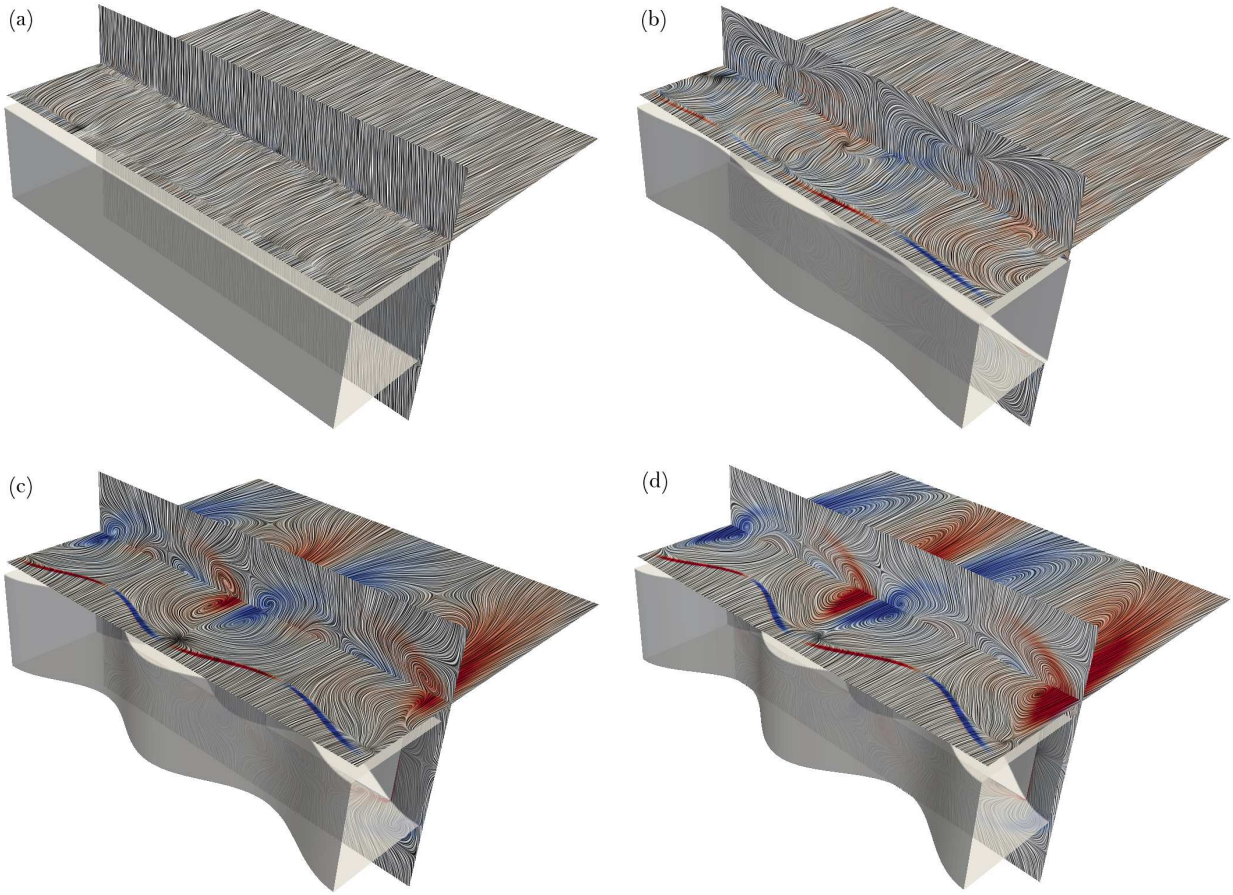

Figure 27: The mean flow streamlines in the $x-z$ and $y-z$ plane which are coloured by the mean crossflow and streamwise vorticity respectively. 10 levels are plotted ranging from -0.3 to 0.3, with red corresponding to positive and blue negative. (a) straight. (b) $w/D = 0.12$. (c) $w/D = 0.36$. (d) $w/D = 0.48$.

reduction in the OASPL becomes 5 dB smaller. This is associated with the growth in the levels at high frequencies at higher Reynolds numbers. The effect of the wavelength on both the peak SPL and the OASPL is found to be small with the differences lower than 2 dB between $\lambda = 2D$ and $4D$ for different Reynolds numbers. Slightly different speed dependences have been found for the straight and wavy cases, which vary from $U^{5.0} - U^{5.8}$ for the peak SPL, and $U^{5.3} - U^{6.1}$ for the OASPL. For all the cases considered, a dipole-like noise pattern was found, with the maximum level in the lift direction and minimum level in the drag direction. The noise levels caused by the spanwise fluctuations are found to be insignificant compared with the lift and drag dipoles.

The current study also analyzed the flow physics associated with the noise reduction. It is found that the fundamental vortex shedding remains with nearly unchanged strengths for the wavy cases with $w/D \leq 0.24$, although the flow tends to become more 3-D. When the amplitude is increased to $w/D = 0.36$, the fundamental vortex shedding is effectively suppressed as the vortex formation is significantly lengthened. This can be attributed to the earlier appearance of the streamwise and crossflow vortices as a consequence of the transportation of the vorticity from the spanwise direction into the other two directions. Turbulence interactions in the wake are also found to be much weaker. Therefore, a significant decrease in the surface fluctuations as well as the far-field noise are found at this waviness amplitude. Further increasing the waviness amplitude to $w/D = 0.48$, both the streamwise and crossflow vortices grow which makes it difficult for the separated shear layer to interact and roll up into the fundamental vortex. The coherent vortex shedding almost vanishes for this amplitude, which leads to a weak broad peak in the far-field noise spectrum. In addition, the wake width expands at the valley and shrinks at the peak.

8. Acknowledgements

All simulations in this paper were run on Iridis 4 Super Computer at the University of Southampton. The authors are also grateful to Arup for financial support.

References

[1] D. P. Lockard, M. R. Khorrami, M. M. Choudhari, F. V. Hutcheson, T. F. Brooks, D. J. Stead, Tandem cylinder noise predictions, AIAA paper 2007-3450, 2007.
[2] D. J. Thompson, E. Latorre Iglesias, X. Liu, J. Zhu, Z. Hu, Recent developments in the prediction and control of aerodynamic noise from high-speed trains, International Journal of Rail Transportation 3 (3) (2015) 119–150.
[3] W. King, E. Pfizenmaier, An experimental study of sound generated by flows around cylinders of different cross-section, Journal of Sound and Vibration 328 (3) (2009) 318–337.
[4] E. Latorre Iglesias, D. Thompson, M. Smith, Experimental study of the aerodynamic noise radiated by cylinders with different cross-sections and yaw angles, Journal of Sound and Vibration 361 (2016) 108–129.
[5] B. Vickery, Fluctuating lift and drag on a long cylinder of square cross-section in a smooth and in a turbulent stream, Journal of Fluid Mechanics 25 (3) (1966) 481–494.
[6] B. Lee, The effect of turbulence on the surface pressure field of a square prism, Journal of Fluid Mechanics 69 (2) (1975) 263–282.
[7] P. Bearman, E. Obasaju, An experimental study of pressure fluctuations on fixed and oscillating square-section cylinders, Journal of Fluid Mechanics 119 (1982) 297–321.
[8] D. Lyn, S. Einav, W. Rodi, J. Park, A laser-doppler velocimetry study of ensemble-averaged characteristics of the turbulent near wake of a square cylinder, Journal of Fluid Mechanics 304 (1995) 285–319.
[9] P. R. Voke, Flow past a square cylinder: test case LES2, Direct and Large–Eddy Simulation II 5 (1997) 355–373.
[10] A. Sohankar, L. Davidson, C. Norberg, Large eddy simulation of flow past a square cylinder: comparison of different subgrid scale models, Journal of Fluids Engineering 122 (1) (2000) 39–47.
[11] F. Trias, A. Gorobets, A. Oliva, Turbulent flow around a square cylinder at Reynolds number 22,000: A dns study, Computers & Fluids 123 (2015) 87–98.
[12] H. Choi, W. P. Jeon, J. Kim, Control of flow over a bluff body, Annual Review Fluid Mechanics 40 (2008) 113–139.
[13] A. Roshko, Experiments on the flow past a circular cylinder at very high Reynolds number, Journal of Fluid Mechanics 10 (3) (1961) 345–356.
[14] P. W. Bearman, J. C. OWen, Reduction of bluff-body drag and suppression of vortex shedding by the introduction of wavy separation lines, Journal of Fluids and Structures 12 (1) (1998) 123–130.
[15] R. M. Darekar, S. J. Sherwin, Flow past a square-section cylinder with a wavy stagnation face, Journal of Fluid Mechanics 426 (2001) 263–295.
[16] K. Lam, Y. Lin, Effects of wavelength and amplitude of a wavy cylinder in cross-flow at low Reynolds numbers, Journal of Fluid Mechanics 620 (2009) 195–220.
[17] H. Park, D. Lee, W.-P. Jeon, S. Hahn, J. Kim, J. Kim, J. Choi, H. Choi, Drag reduction in flow over a two-dimensional bluff body with a blunt trailing edge using a new passive device, Journal of Fluid Mechanics 563 (2006) 389–414.
[18] J. Owen, A. Szewczyk, P. Bearman, Suppression of karman vortex shedding, Physics of Fluids 12 (9) (2000) S9–S9.
[19] M. Ikeda, Study of the aerodynamic noise characteristics of bluff bodies as a pantograph member, in: Proceedings of Forum Acusticum, Sevilla, Spain, 2002.
[20] T. Takaishi, M. Ikeda, C. Kato, Method of evaluating dipole sound source in a finite computational domain, The Journal of the Acoustical Society of America 116 (3) (2004) 1427–1435.
[21] T. Sueki, M. Ikeda, T. Takaishi, T. Kurita, H. Yamada, Reduction of aerodynamic noise from high-speed pantograph using porous materials, Journal of Environment and Engineering 5 (3) (2010) 469–484.
[22] I. Ver, Noise of jet engine test cells, in: Jet Engine Test Cell Meeting, Naval Facilities Engineering Command, Alexandria, VA, 1987.
[23] A. S. Hersh, P. T. Soderman, R. E. Hayden, Investigation of acoustic effects of leading-edge serrations on airfoils, Journal of Aircraft 11 (4) (1974) 197–202.
[24] R. E. Arndt, T. Nagel, Effect of leading edge serrations on noise radiation from a model rotor, AIAA Paper 655,1972.
[25] R. E. Longhouse, Vortex shedding noise of low tip speed, axial flow fans, Journal of Sound and vibration 53 (1) (1977) 25–46.
[26] A. S. Hersh, R. E. Hayden, Aerodynamic sound radiation from lifting surfaces with and without leading-edge serrations, NASA CR-114370,1971.
[27] K. L. Hansen, N. Rostamzadeh, R. M. Kelso, B. B. Dally, Evolution of the streamwise vortices generated between leading edge tubercles, Journal of Fluid Mechanics 788 (2016) 730–766.
[28] R. Pérez-Torró, J. W. Kim, A large-eddy simulation on a deep-stalled aerofoil with a wavy leading edge, Journal of Fluid Mechanics 813 (2017) 23–52.
[29] J. W. Kim, S. Haeri, P. F. Joseph, On the reduction of aerofoil–turbulence interaction noise associated with wavy leading edges, Journal of Fluid Mechanics 792 (2016) 526–552.
[30] P. Chaitanya, P. Joseph, S. Narayanan, C. Vanderwel, J. Turner, J.-W. Kim, B. Ganapathisubramani, Performance and mechanism of sinusoidal leading edge serrations for the reduction of turbulence–aerofoil interaction noise, Journal of Fluid Mechanics 818 (2017) 435–464.
[31] J. M. Turner, J. W. Kim, Aeroacoustic source mechanisms of a wavy leading edge undergoing vortical disturbances, Journal of Fluid Mechanics 811 (2017) 582–611.
[32] A. S. Lau, S. Haeri, J. W. Kim, The effect of wavy leading edges on aerofoil–gust interaction noise, Journal of Sound and Vibration 332 (24) (2013) 6234–6253.

[33] V. Clair, C. Polacsek, T. Le Garrec, G. Reboul, M. Gruber, P. Joseph, Experimental and numerical investigation of turbulence–airfoil noise reduction using wavy edges, AIAA Journal 51 (11) (2013) 2695–2713.
[34] T. Colonius, S. K. Lele, Computational aeroacoustics: progress on nonlinear problems of sound generation, Progress in Aerospace Sciences 40 (6) (2004) 345–416.
[35] X. Liu, D. J. Thompson, Z. Hu, V. Jurdic, Aerodynamic noise from a train pantograph, in: Proceedings of 21st International Congress on Sound and Vibration, Beijing, China, 2014.
[36] P. R. Spalart, Strategies for turbulence modelling and simulations, International Journal of Heat and Fluid Flow 21 (3) (2000) 252–263.
[37] J. Fröhlich, D. von Terzi, Hybrid LES/RANS methods for the simulation of turbulent flows, Progress in Aerospace Sciences 44 (5) (2008) 349–377.
[38] P. R. Spalart, S. Deck, M. Shur, K. Squires, M. K. Strelets, A. Travin, A new version of detached–eddy simulation, resistant to ambiguous grid densities, Theoretical and computational fluid dynamics 20 (3) (2006) 181–195.
[39] J. F. Williams, D. L. Hawkings, Sound generation by turbulence and surfaces in arbitrary motion, Philosophical Transactions of the Royal Society of London A: Mathematical, Physical and Engineering Sciences 264 (1151) (1969) 321–342.
[40] M. J. Lighthill, On sound generated aerodynamically. I. General theory, Proceedings of the Royal Society of London A: Mathematical, Physical and Engineering Sciences 211 (1107) (1952) 564–587.
[41] N. Curle, The influence of solid boundaries upon aerodynamic sound, Proceedings of the Royal Society of London A: Mathematical, Physical and Engineering Sciences 231 (1187) (1955) 505–514.
[42] D. Crighton, Basic principles of aerodynamic noise generation, Progress in Aerospace Sciences 16 (1) (1975) 31–96.
[43] C. Mockett, R. Perrin, T. Reimann, M. Braza, F. Thiele, Analysis of detached-eddy simulation for the flow around a circular cylinder with reference to piv data, in: IUTAM Symposium on Unsteady Separated Flows and their Control, Springer, 2009, pp. 417–427.
[44] C. Norberg, Flow around rectangular cylinders: pressure forces and wake frequencies, Journal of Wind Engineering and Industrial Aerodynamics 49 (1-3) (1993) 187–196.
[45] B. Lee, Some effects of turbulence scale on the mean forces on a bluff body, Journal of Wind Engineering and Industrial Aerodynamics 1 (1975) 361–370.
[46] Y. Nakamura, T. Mizota, Unsteady lifts and wakes of oscillating rectangular prisms, Journal of the Engineering Mechanics Division 101 (6) (1975) 855–871.
[47] Y. Otsuki, K. Washizu, H. Tomizawa, A. Ohya, A note on the aeroelastic instability of a prismatic bar with square section, Journal of Sound and Vibration 34 (2) (1974) 233–248.
[48] Z. Hu, C. L. Morfey, N. D. Sandham, Wall pressure and shear stress spectra from direct simulations of channel flow, AIAA Journal 44 (7) (2006) 1541–1549.
[49] T. Chong, P. Joseph, P. Davies, Design and performance of an open jet wind tunnel for aero-acoustic measurement, Applied Acoustics 70 (4) (2009) 605–614.
[50] W. King III, E. Pfizenmaier, M. Herrmann, L. Neuhaus, An experimental study of sound generated by flow interactions with cylinders., Deufrako K2 report,1997.
[51] S. Yamada, H. Fujita, Y. Maruta, H. Maki, J. Shiraishi, Experimental study on aerodynamic noise generated from two-dimensional models (2^{nd} report, effect of the angle of inclination of circular cylinders and the angle of attack of square cylinders to aerodynamic noise), Trans. JSME 63 (610) (1997) 1974–1979.
[52] M. S. Bloor, The transition to turbulence in the wake of a circular cylinder, Journal of Fluid Mechanics 19 (2) (1964) 290–304.
[53] C. W. Hamman, J. C. Klewicki, R. M. Kirby, On the lamb vector divergence in Navier–Stokes flows, Journal of Fluid Mechanics 610 (2008) 261–284.
[54] M. S. Howe, Theory of vortex sound, Cambridge University Press, 2003.